

# Efficacy and safety assessment of a TRAF6-targeted nanoimmunotherapy in atherosclerotic mice and non-human primates

Marnix Lameijer<sup>1,2</sup>, Tina Binderup<sup>3</sup>, Mandy M. T. van Leent<sup>1,2</sup>, Max L. Senders<sup>1,2</sup>, Francois Fay<sup>1</sup>, Joost Malkus<sup>1</sup>, Brenda L. Sanchez-Gaytan<sup>1</sup>, Abraham J. P. Teunissen<sup>1</sup>, Nicolas Karakatsanis<sup>1</sup>, Philip Robson<sup>1</sup>, Xianxiao Zhou<sup>4</sup>, Yuxiang Ye<sup>5</sup>, Gregory Wojtkiewicz<sup>5</sup>, Jun Tang<sup>6</sup>, Tom T. P. Seijkens<sup>2</sup>, Jeffrey Kroon<sup>7</sup>, Erik S. G. Stroes<sup>7</sup>, Andreas Kjaer<sup>3</sup>, Jordi Ochando<sup>8</sup>, Thomas Reiner<sup>6</sup>, Carlos Pérez-Medina<sup>1</sup>, Claudia Calcagno<sup>1</sup>, Edward A. Fischer<sup>9</sup>, Bin Zhang<sup>4</sup>, Ryan E. Temel<sup>10</sup>, Filip K. Swirski<sup>5</sup>, Matthias Nahrendorf<sup>5</sup>, Zahi A. Fayad<sup>1</sup>, Esther Lutgens<sup>2,11</sup>, Willem J. M. Mulder<sup>1,2\*</sup> and Raphaël Duivenvoorden<sup>1,7,12\*</sup>

**Macrophage accumulation in atherosclerosis is directly linked to the destabilization and rupture of plaque, causing acute atherothrombotic events. Circulating monocytes enter the plaque and differentiate into macrophages, where they are activated by CD4<sup>+</sup> T lymphocytes through CD40–CD40 ligand signalling. Here, we report the development and multiparametric evaluation of a nanoimmunotherapy that moderates CD40–CD40 ligand signalling in monocytes and macrophages by blocking the interaction between CD40 and tumour necrosis factor receptor-associated factor 6 (TRAF6). We evaluated the biodistribution characteristics of the nanoimmunotherapy in apolipoprotein E-deficient (*Apoe*<sup>-/-</sup>) mice and in non-human primates by in vivo positron-emission tomography imaging. In *Apoe*<sup>-/-</sup> mice, a 1-week nanoimmunotherapy treatment regimen achieved significant anti-inflammatory effects, which was due to the impaired migration capacity of monocytes, as established by a transcriptome analysis. The rapid reduction of plaque inflammation by the TRAF6-targeted nanoimmunotherapy and its favourable toxicity profiles in both mice and non-human primates highlights the translational potential of this strategy for the treatment of atherosclerosis.**

The recruitment of monocytes to the vessel wall is a key contributing process to macrophage accumulation in the atherosclerotic plaque<sup>1</sup>. This process is directly linked to the development of atherothrombotic events<sup>1</sup>.

As early as in the 1990s, it was recognized that the activation of plaque monocytes and macrophages by CD4<sup>+</sup> T lymphocytes via CD40–CD40 ligand (CD40–CD40L) signalling plays a central role in abetting plaque inflammation<sup>2</sup>, paving the way for new immunotherapeutic avenues<sup>3–6</sup>. Subsequent studies have revealed that TRAF6 is of specific importance in propelling the signalling cascade of CD40 inside monocytes and macrophages<sup>7</sup>. Deficient CD40–TRAF6 interactions in myeloid cells has been shown to decrease monocyte recruitment to plaques and to abolish atherosclerotic plaque formation in *Apoe*<sup>-/-</sup> mice<sup>7</sup>.

The goal of this study was to develop and multiparametrically evaluate a targeted nanoimmunotherapy that specifically blocks the CD40–TRAF6 interaction in monocytes and macrophages.

For this purpose, we incorporated a recently developed small-molecule inhibitor of the CD40–TRAF6 interaction in reconstituted high-density lipoprotein (HDL), which we call TRAF6i–HDL<sup>8,9</sup>. We show in an *Apoe*<sup>-/-</sup> mouse model of atherosclerosis that TRAF6i–HDL is taken up by monocytes and macrophages, while lymphocytes do not take up the nanoimmunotherapy. Fully integrated three-dimensional (3D) positron-emission tomography with magnetic resonance imaging (PET/MRI) methods were developed to non-invasively study the pharmacokinetics of TRAF6i–HDL and its biodistribution in non-human primates. Therapeutic studies carried out in atherosclerotic mice revealed the ability of the TRAF6i–HDL nanoimmunotherapy to rapidly decrease monocyte recruitment, thereby decreasing plaque inflammation. In line with these findings, a whole transcriptome analysis and in vitro assays indicated that cell migration was among the affected cellular processes. Finally, the safety of TRAF6i–HDL was established in both atherosclerotic mice and non-human primates.

<sup>1</sup>Translational and Molecular Imaging Institute, Icahn School of Medicine at Mount Sinai, New York, NY, USA. <sup>2</sup>Department of Medical Biochemistry, Academic Medical Center, Amsterdam, The Netherlands. <sup>3</sup>Cluster for Molecular Imaging and Department of Clinical Physiology, Nuclear Medicine and PET, Rigshospitalet and University of Copenhagen, Copenhagen, Denmark. <sup>4</sup>Department of Genetics and Genomic Sciences, Icahn School of Medicine at Mount Sinai, New York, NY, USA. <sup>5</sup>Center for Systems Biology, Massachusetts General Hospital, Harvard Medical School, Boston, MA, USA. <sup>6</sup>Department of Radiology, Memorial Sloan Kettering Cancer Center, New York, NY, USA. <sup>7</sup>Department of Vascular Medicine, Amsterdam Cardiovascular Sciences, Academic Medical Center, Amsterdam, The Netherlands. <sup>8</sup>Immunology Institute, Department of Oncological Sciences, Icahn School of Medicine at Mount Sinai, New York, NY, USA. <sup>9</sup>Department of Medicine (Cardiology) and Cell Biology, Marc and Ruti Bell Program in Vascular Biology, NYU School of Medicine, New York, NY, USA. <sup>10</sup>Saha Cardiovascular Research Center and Department of Pharmacology and Nutritional Sciences, University of Kentucky, Lexington, KY, USA. <sup>11</sup>Institute for Cardiovascular Prevention, Ludwig-Maximilians University, Munich, Germany. <sup>12</sup>Department of Nephrology, Academic Medical Center, Amsterdam, The Netherlands. \*e-mail: [willem.mulder@mssm.edu](mailto:willem.mulder@mssm.edu); [r.duivenvoorden@amc.uva.nl](mailto:r.duivenvoorden@amc.uva.nl)

## Results

**TRAF6i-HDL characteristics.** The aim of this study was to decrease plaque inflammation by moderating CD40-CD40L signalling in monocytes and macrophages via site-specific blockade of the interaction between CD40 and TRAF6. TRAF6i-HDL (schematically shown in Fig. 1a) was constructed from human apolipoprotein A-I (apoA-I) and the phospholipids 1-myristoyl-2-hydroxy-*sn*-glycero-phosphocholine (MHPC) and 1,2-dimyristoyl-*sn*-glycero-3-phosphatidylcholine (DMPC), in which a lipophilic small-molecule inhibitor (SMI 6877002) of the CD40-TRAF6 interaction was encapsulated<sup>8</sup>. SMI 6877002 binds to the TRAF6-binding site on CD40 and not to the TRAF6-binding sites on the interleukin-1R-associated kinases (IRAKs), leaving interleukin-1 receptor (IL-1)-Toll-like receptor signalling unaffected<sup>8</sup>. The mean size and polydispersity, as determined by dynamic light scattering, of the different TRAF6i-HDL batches used in this study were  $20.7 \pm 3.0$  nm and  $0.26 \pm 0.07$  ( $n = 10$  batches), respectively. Transmission electron micrographs are shown in Supplementary Fig. 1. TRAF6i-HDL variants, incorporating fluorescent dyes (DiO or DiR) or Zirconium-89 (<sup>89</sup>Zr)-radiolabelled phospholipids, were synthesized to enable their detection by fluorescence techniques, PET, gamma counting and autoradiography. Additional data on nanoparticle characteristics, such as stability, drug release and labelling, are provided in Supplementary Fig. 2.

**Study outline.** A schematic overview of the study design is shown in Fig. 1b. First, we studied the pharmacokinetics, biodistribution, and atherosclerotic plaque monocyte and macrophage targeting efficiency of TRAF6i-HDL in atherosclerotic mice. In parallel, we developed an in vivo PET/MRI protocol to longitudinally study the biodistribution of TRAF6i-HDL in non-human primates. Subsequently, in atherosclerotic mice, plaque regression efficacy of a 1-week TRAF6i-HDL regimen involving four intravenous infusions was studied by immunohistochemistry. The effects of TRAF6i-HDL on the immune system were also studied. To shed light on the therapeutic mechanism, whole transcriptome analysis of plaque macrophages, in vitro transendothelial migration assays and in vivo imaging of protease activity in the aortic sinus area were performed. Finally, the safety of the TRAF6i-HDL nanoimmunotherapy was established in atherosclerotic mice and in non-human primates.

**Pharmacokinetics and biodistribution studies in *ApoE*<sup>-/-</sup> mice.** To investigate its pharmacokinetics and biodistribution, *ApoE*<sup>-/-</sup> mice received a single infusion of <sup>89</sup>Zr-radiolabelled TRAF6i-HDL (<sup>89</sup>Zr-TRAF6i-HDL). Blood radioactivity clearance of <sup>89</sup>Zr-TRAF6i-HDL was measured over 24 h, and data were fitted using a two-phase decay non-linear regression. The weighted blood half-life ( $t_{1/2}$ ) was finally calculated to be 124.4 min based on a  $t_{1/2}$ -fast of 13.7 min and a  $t_{1/2}$ -slow of 195 min (Fig. 1c).

Biodistribution was evaluated by in vivo PET with computed tomography (CT) imaging (Fig. 1d) and validated by ex vivo gamma counting, the latter expressed as a percentage of injected dose per gram of tissue (%ID g<sup>-1</sup>; Fig. 1e). As expected, PET/CT imaging showed that <sup>89</sup>Zr-TRAF6i-HDL primarily accumulated in the liver, spleen and kidneys, organs known to take up and metabolize HDL. Gamma counting data confirmed these results, showing <sup>89</sup>Zr-TRAF6i-HDL uptake of 12.8 %ID g<sup>-1</sup> in the liver, 8.9 %ID g<sup>-1</sup> in the spleen and 7.9 %ID g<sup>-1</sup> in the kidneys. In comparison, the heart, a similar sized organ, only contained 1.1 %ID g<sup>-1</sup> (Fig. 1e). Ex vivo near infrared fluorescence (NIRF) imaging performed 24 h after infusion corroborated the PET/CT and gamma counting observations, showing that TRAF6i-HDL accumulates primarily in the liver, spleen and kidneys (Fig. 1f).

Flow cytometry analyses revealed that Ly6C<sup>hi</sup> monocytes and macrophages in blood, bone marrow and spleen took up DiO

core-labelled TRAF6i-HDL. Neutrophils, Ly6C<sup>lo</sup> monocytes and dendritic cells also took up DiO-TRAF6i-HDL, while lineage-positive CD11b<sup>-</sup> cells (all non-myeloid cells) did not (Supplementary Fig. 3), indicative of myeloid cell specificity.

**TRAF6i-HDL accumulation in atherosclerotic lesions.** Ex vivo gamma counting of whole aortas showed that 1.3 %ID g<sup>-1</sup> of <sup>89</sup>Zr-TRAF6i-HDL had accumulated 24 h after infusion (Fig. 1e). Looking specifically at <sup>89</sup>Zr-TRAF6i-HDL distribution throughout the aorta, the uptake was highest in the aortic sinus area (Fig. 1g), which is the preferential site of plaque development in this mouse model. While only accounting for 6.4% of the total area, the aortic sinus area generated approximately 29% of the signal, corresponding to 5.9 %ID g<sup>-1</sup> (Fig. 1d). NIRF imaging showed similar preferential accumulation of DiR-labelled TRAF6i-HDL in the aortic sinus area (Fig. 1h).

The cell specificity of DiO-labelled TRAF6i-HDL uptake in aortic plaques was assessed by flow cytometry. We found that 86% of macrophages and 81% of Ly6C<sup>hi</sup> monocytes had taken up DiO-TRAF6i-HDL, whereas lineage-positive cells (all non-myeloid cells) had taken up virtually none (Fig. 1i). Furthermore, the majority of neutrophils (64%) and dendritic cells (61%) in the aortic plaque were found to contain DiO-TRAF6i-HDL (Supplementary Fig. 3). These results mirror our findings in blood, bone marrow and spleen, showing that cells of the myeloid lineage, in particular the Ly6C<sup>hi</sup> monocyte subset and macrophages, show a high uptake of TRAF6i-HDL nanoparticles.

## PET/MRI-facilitated pharmacokinetics and biodistribution studies in non-human primates.

To assess biodistribution in non-human primates, we developed a fully integrated 3D PET/MRI protocol that enables dynamic and longitudinal imaging of <sup>89</sup>Zr-TRAF6i-HDL. Six non-human primates were subjected to full-body PET/MRI (see Supplementary Video 1 for 3D rendered MRI data) after intravenous administration of <sup>89</sup>Zr-TRAF6i-HDL. The animals were dynamically imaged over the course of the first hour post administration, while subsequent static scans were performed at 1, 24, 48 and 72 h. Dynamic PET imaging showed rapid radioactivity accumulation in the liver, spleen and kidneys, followed by a significant uptake in the bone marrow (Fig. 2a, Supplementary Video 2). One hour post injection, PET images revealed a strong kidney <sup>89</sup>Zr-TRAF6i-HDL signal, followed by the liver and spleen (Fig. 2a). At 24, 48 and 72 h, radioactivity was found accumulated mostly in the liver and spleen (Fig. 2b). After the animals were euthanized at the 72 h time point, tissue gamma counting showed that the largest amount of the injected dose (%ID g<sup>-1</sup>) could be traced back to the liver and spleen, followed by the kidneys, corroborating the in vivo PET/MRI findings (Fig. 2c, Supplementary Fig. 4a,b). Blood was collected at different time points and the data were fitted using a two-phase decay non-linear regression. The  $t_{1/2}$ -fast was 14.2 min and the  $t_{1/2}$ -slow was 513 min, resulting in a weighted blood  $t_{1/2}$  of 272 min (Fig. 2d).

**In vivo effects of TRAF6i-HDL on plaque inflammation.** To assess the therapeutic efficacy of TRAF6i-HDL, we used 20-week-old *ApoE*<sup>-/-</sup> mice that had been fed a high-cholesterol diet for 12 weeks to develop atherosclerotic lesions. While all mice remained on a high-cholesterol diet, they received four intravenous infusions of control PBS, control HDL nanoparticles or TRAF6i-HDL over 7 days. The CD40-TRAF6 inhibitor dose administered per infusion was 5 mg kg<sup>-1</sup>. To limit a concomitant therapeutic effect of apoA-I itself, we used a low apoA-I dose of 9 mg kg<sup>-1</sup>. All mice were euthanized 24 h after the final infusion.

For the first experiment, we performed quantitative histological analysis of plaques in the aortic sinus area in mice treated with control, HDL or TRAF6i-HDL ( $n = 10$  per group). Cross-sections

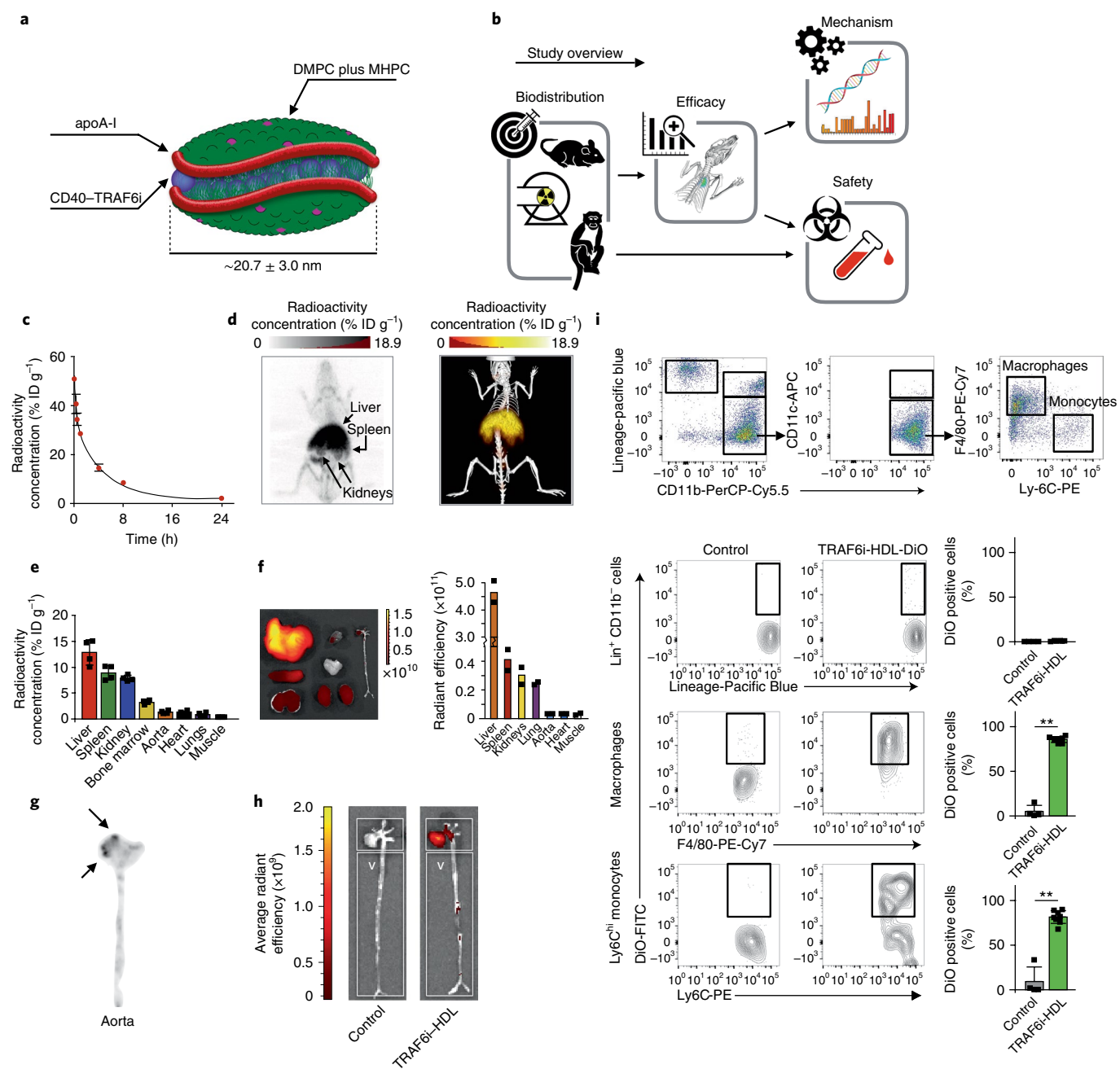


**Fig. 1 | TRAF6i-HDL biodistribution and uptake.** **a**, A schematic representation of TRAF6i-HDL, which was constructed by combining human apoA-I, the lipids DMPC and MHPC, and a small-molecule inhibitor of the CD40-TRAF6 interaction. **b**, Study overview showing the subsequent steps that were taken to investigate the in vivo behaviour and therapeutic efficacy of TRAF6i-HDL. Eight-week-old *ApoE*<sup>-/-</sup> mice were fed a high-cholesterol diet for 12 weeks and then given an intravenous injection of <sup>89</sup>Zr-radiolabelled, DiR core-labelled or DiO core-labelled TRAF6i-HDL nanoparticles. Twenty-four hours later, mice underwent PET/CT imaging or were euthanized for ex vivo NIRF imaging or flow cytometry analysis. **c**, Pharmacokinetics of <sup>89</sup>Zr-labelled TRAF6i-HDL in *ApoE*<sup>-/-</sup> mice (*n* = 3), showing the blood decay curve. **d**, Whole-body 3D rendered PET/CT fusion image at 24 h post administration showing the highest uptake in the liver, spleen and kidneys. **e**, Gamma counting of the distribution of <sup>89</sup>Zr-labelled TRAF6i-HDL at 24 h post administration (*n* = 4). Bars represent the mean and standard error of the mean. **f**, Biodistribution 24 h after infusion of DiO core-labelled TRAF6i-HDL in *ApoE*<sup>-/-</sup> mice (*n* = 2). Ex vivo NIRF imaging showed that the nanoparticles accumulate mostly in the liver, spleen and kidneys. **g**, Autoradiography of the aorta showed visible TRAF6i-HDL accumulation in the aortic root (*n* = 3), which is the preferential location of atherosclerosis development in the mouse model. The arrows indicate the aortic sinus area. **h**, NIRF imaging of DiR core-labelled TRAF6i-HDL distribution in mouse aorta (*n* = 2) showed accumulation of TRAF6i-HDL in the aortic root area. **i**, Flow cytometry data of whole mouse aortas (*n* = 8) with DiO-labelled TRAF6i-HDL (TRAF6i-HDL-DiO) showed the high targeting efficiency of macrophages (*P* = 6.4 × 10<sup>-3</sup>) and Ly6C<sup>hi</sup> monocytes (*P* = 6.5 × 10<sup>-3</sup>), while lineage-positive CD11b<sup>-</sup> cells did not take up nanoparticles. \*\**P* < 0.01. *P* values were calculated using Mann-Whitney U tests (two-sided). Bars represent the mean and standard error of the mean.

were stained with haematoxylin and eosin (H&E) and Sirius Red (collagen), and immunostained for Mac3 (macrophages) and Ki67 (proliferating cells). No significant difference in plaque size or

collagen content was observed among the groups (Fig. 3a). However, in TRAF6i-HDL-treated mice, the percentage of the Mac3-positive area was markedly decreased by 36% (*P* = 0.001) and 37% (*P* < 0.001)

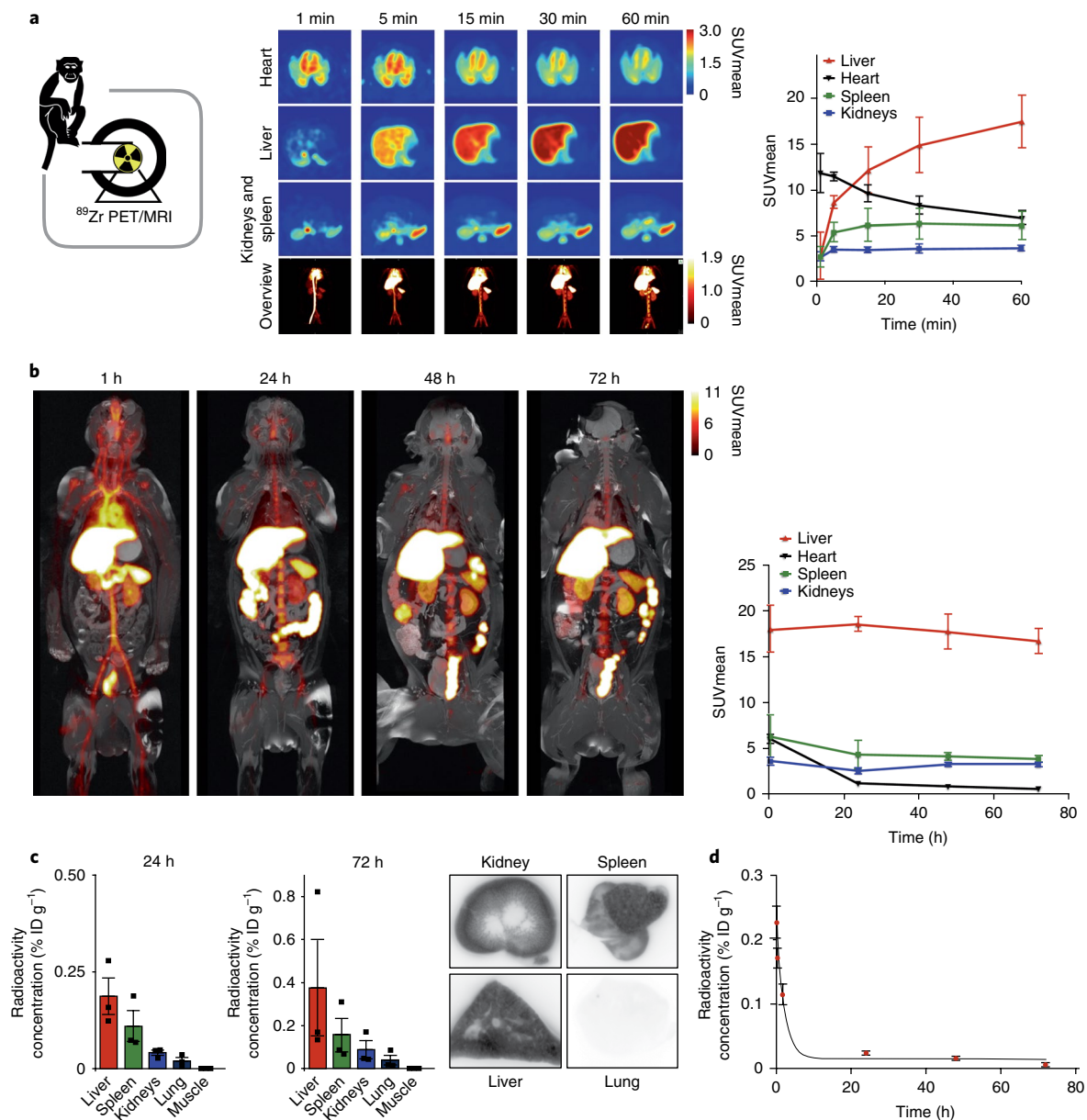


**Fig. 2 | TRAF6i-HDL biodistribution in non-human primates.** Six non-human primates were infused with  $^{89}\text{Zr}$ -labelled TRAF6i-HDL ( $1\text{ mg kg}^{-1}$ ). Dynamic PET images were acquired within 60 min after infusion. Static PET/MRI scans were performed at 24, 48 and 72 h (see Supplementary Video 1 for 3D rendered MRI data). Non-human primates were euthanized after 72 h. Organs were collected for ex vivo analysis. **a**, Dynamic PET images at 1, 5, 15, 30 and 60 min ( $n=3$ ). Images are split up to visualize liver and other organs separately. The graph shows the quantified uptake in the represented organs at the different time points (see Supplementary Video 2 for a 3D representation of the distribution at 60 min). SUVmean, mean standardized uptake value. **b**, Static PET/MR images at 24, 48 and 72 h show the distribution and accumulation of TRAF6i-HDL. The graph shows the quantified uptake in the represented organs at the different time points ( $n=3$  per time point). **c**, Gamma counting distribution in non-human primates at 24 and 72 h post administration of  $^{89}\text{Zr}$ -TRAF6i-HDL ( $n=3$ ). Bars represent the mean. **d**, Blood time-activity curve for  $^{89}\text{Zr}$ -TRAF6i-HDL in non-human primates ( $n=3$  per time point). Bars represent the standard error of the mean.

compared with the control and HDL groups, respectively (Fig. 3b). As a result, the Mac3 to collagen ratio in the plaque was favourably shifted towards a more stable plaque phenotype in the TRAF6i-HDL group, as the ratio was decreased by 31% ( $P<0.001$ ) and 36% ( $P=0.004$ ) compared with the control and HDL groups, respectively (Fig. 3b). The number of proliferating macrophages was similar in all groups (Fig. 3a), indicating that the observed decrease in plaque macrophages was not caused by a decrease in local proliferation of macrophages. Previous studies have shown that in addition to monocyte recruitment, local macrophage proliferation plays a pivotal role in fuelling plaque inflammation<sup>10</sup>.

Next, we focused on quantifying the aorta macrophage content by flow cytometry analysis of whole aortas. Again, 20-week-old *Apoe*<sup>-/-</sup> mice fed a high-cholesterol diet were treated with control ( $n=27$ ), HDL ( $n=27$ ) or TRAF6i-HDL ( $n=27$ ). The aorta macrophage content decreased markedly in the TRAF6i-HDL-treated group by 66% and 67% ( $P<0.001$  for both comparisons) compared with the control and HDL groups, respectively (Fig. 4a). Furthermore, in the TRAF6i-HDL-treated group, aorta T-lymphocyte content was decreased by 65% and 49% compared with the control and HDL groups, respectively (Supplementary Fig. 5). Altogether, these data indicate a potent anti-inflammatory

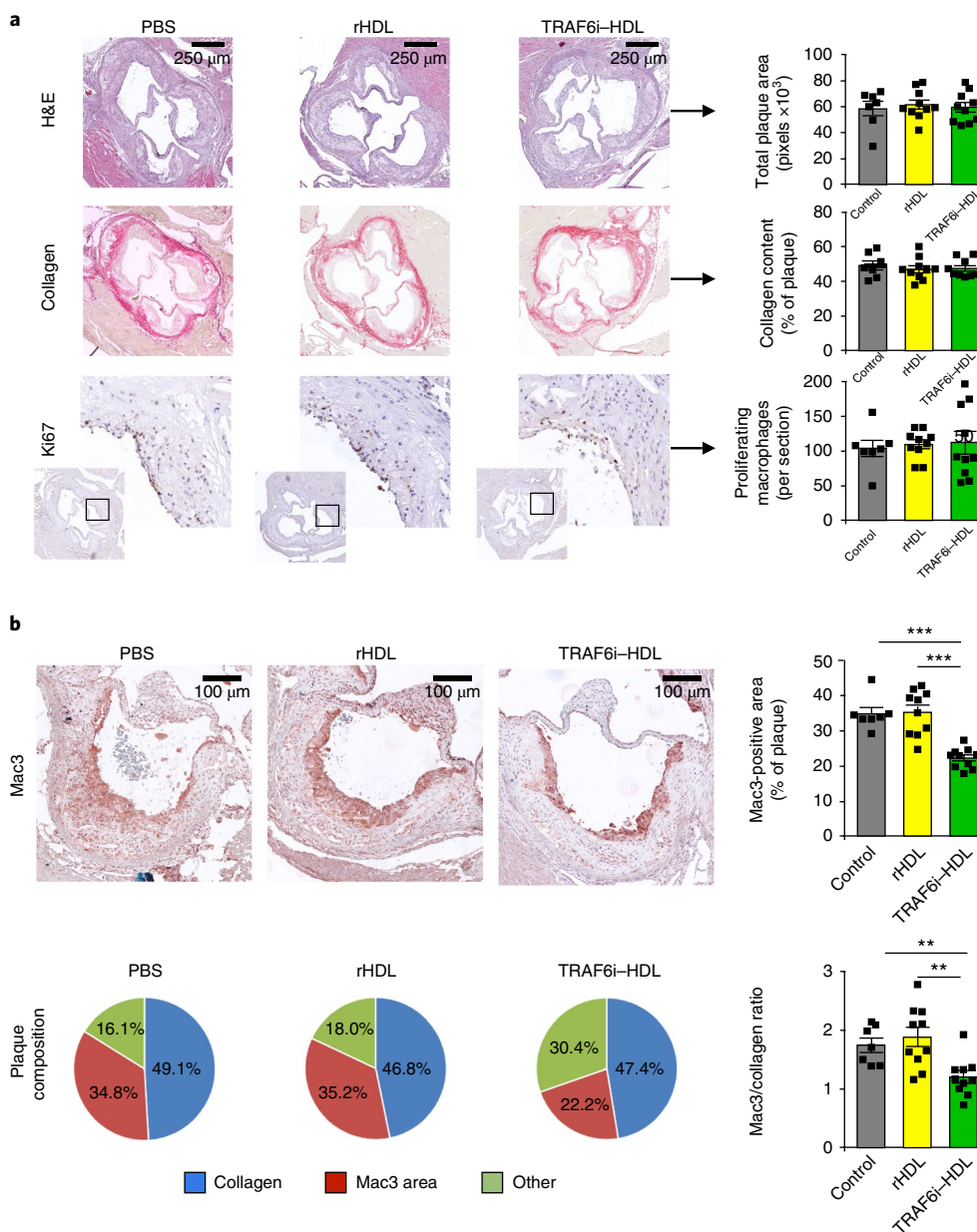


**Fig. 3 | TRAF6i-HDL therapy decreases plaque macrophage content as assessed by histology.** Eight-week-old *ApoE*<sup>-/-</sup> mice were fed a high-cholesterol diet for 12 weeks and subsequently received four intravenous injections of control (*n* = 10), rHDL (*n* = 10) or TRAF6i-HDL (*n* = 10) over the course of 7 days. Twenty-four hours after the last injection, aortic roots were sectioned (4 μM) and stained using (immuno)histochemistry methods. **a**, Aortic roots show no difference in plaque size (H&E), collagen content (Sirius Red) or number of proliferating cells (Ki67 staining). **b**, Mac3 staining of aortic roots shows a marked decrease in macrophage-positive area in the TRAF6i-HDL group compared with the control and rHDL groups (*P* = 6.4 × 10<sup>-4</sup> and *P* = 2.1 × 10<sup>-4</sup>, respectively; Kruskal-Wallis *P* = 1.4 × 10<sup>-4</sup>; *n* = 10 per group). The macrophage to collagen ratio was also decreased in the TRAF6i-HDL group compared with the control and rHDL groups (*P* = 2.5 × 10<sup>-3</sup> and *P* = 5.2 × 10<sup>-3</sup>, respectively; Kruskal-Wallis *P* = 2.9 × 10<sup>-3</sup>; *n* = 10 per group). For all figures, bars represent the mean and standard error of the mean unless otherwise stated. \*\**P* < 0.01 and \*\*\**P* < 0.001. *P* values were calculated using Mann-Whitney U tests (two-sided).

effect of TRAF6i-HDL in atherosclerotic plaques after 1 week of therapy.

Since we had already observed that the number of proliferating Ki67<sup>+</sup> macrophages was not affected by the therapy, we hypothesized that the decrease in plaque macrophage content and inflammation is caused by decreased monocyte recruitment<sup>11,12</sup>. To further investigate this hypothesis, we first quantified aortic Ly6C<sup>hi</sup> monocytes in the same flow cytometry experiment as the one in which we measured macrophage content. We observed that the decrease in macrophages was paralleled by a 49% and 52% (*P* < 0.001 for both

comparisons) decrease in Ly6C<sup>hi</sup> monocytes in the aorta compared with the control and HDL groups, respectively (Fig. 4a). Interestingly, the reduction in aortic Ly6C<sup>hi</sup> monocyte content could not be explained by a systemic decrease in Ly6C<sup>hi</sup> monocytes (Fig. 4b). Instead, we observed an increase in the percentage of Ly6C<sup>hi</sup> monocytes in the bone marrow, spleen and blood. The cause of this relative increase is unclear. Enhanced monocyte survival is unlikely to be the cause, since stimulation of CD40 signalling is known to enhance monocyte survival, whereas we inhibited the CD40 signalling pathway<sup>13</sup>. Increased monocyte production in the bone marrow

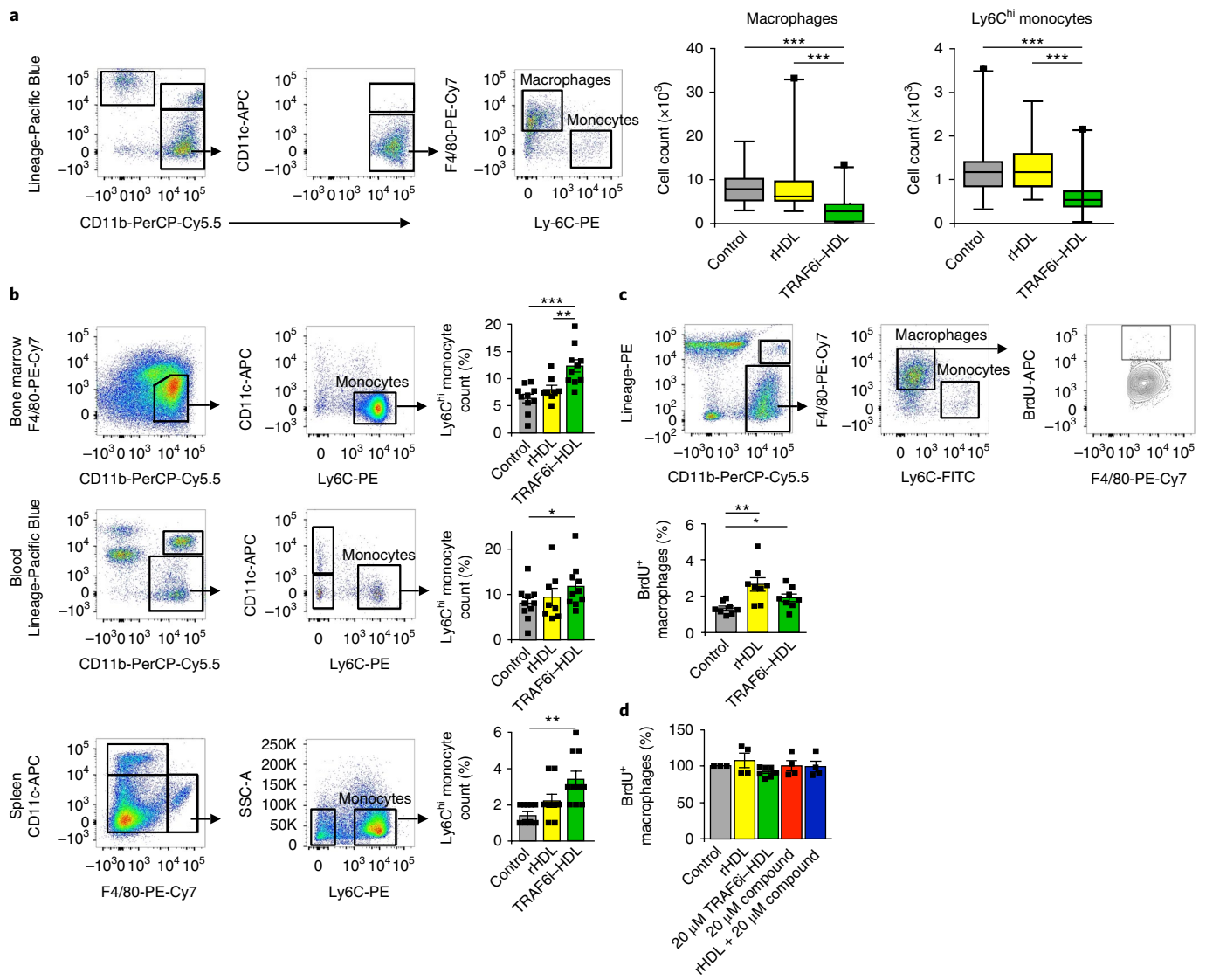


**Fig. 4 | TRAF6i-HDL decreases plaque inflammation due to impaired Ly6C<sup>hi</sup> monocyte recruitment.** Eight-week-old *Apoe*<sup>-/-</sup> mice fed a high-cholesterol diet for 12 weeks were treated with four intravenous injections of control (PBS), rHDL or TRAF6i-HDL for 1 week. **a**, Flow cytometry analysis of whole aortas showed a significant reduction in the number of macrophages in the TRAF6i-HDL-treated group ( $n=27$ ) compared with the control ( $n=27$ ,  $P=2.0 \times 10^{-6}$ ) and rHDL ( $n=26$ ,  $P=1.0 \times 10^{-5}$ , Kruskal-Wallis  $P=6.0 \times 10^{-7}$ ) groups. Ly6C<sup>hi</sup> monocytes are also markedly reduced in the TRAF6i-HDL group compared with the control ( $n=27$ ,  $P=8.9 \times 10^{-5}$ ) and rHDL ( $n=26$ ,  $P=5.6 \times 10^{-5}$ ) groups, thus indicating impairment of Ly6C<sup>hi</sup> monocyte recruitment (Kruskal-Wallis  $P=2.4 \times 10^{-5}$ ). The box plots indicate the minimum and maximum values (whiskers), the 25th to 75th percentiles (box) and the median (line in the box). **b**, Flow cytometry analysis of bone marrow, blood and spleen showed that the decrease in plaque Ly6C<sup>hi</sup> monocyte content could not be attributed to systemic decreases in Ly6C<sup>hi</sup> monocytes ( $n=8-10$  per group, single experiment). In fact, Ly6C<sup>hi</sup> monocytes were higher in the bone marrow ( $P=5.8 \times 10^{-4}$ ), blood ( $P=2.7 \times 10^{-2}$ ) and spleen ( $P=1.5 \times 10^{-3}$ ) in the TRAF6i-HDL group compared with the control group. There was no significant difference in Ly6C<sup>hi</sup> monocytes between TRAF6i-HDL and rHDL in the blood ( $P=0.31$ ) and spleen ( $P=0.07$ ), while there was a difference between these groups in the bone marrow ( $P=5.5 \times 10^{-3}$ ). **c**, In vivo BrdU incorporation experiment showed no inhibiting effect of TRAF6i-HDL ( $n=8$ ) on plaque macrophage proliferation. BrdU incorporation was higher in the rHDL and TRAF6i-HDL groups compared with the control group ( $P=3.3 \times 10^{-3}$  and  $P=2.7 \times 10^{-2}$ ). **d**, In vitro experiments ( $n=3$ ) of BrdU incorporation in RAW264.7 macrophages treated for 24 h with control, rHDL, TRAF6i-HDL, bare CD40-TRAF6 small-molecule inhibitor or a combination of rHDL + bare CD40-TRAF6 small-molecule inhibitor showed no effect on macrophage proliferation. For all figures, the means and standard errors of the mean are shown unless otherwise stated. \* $P < 0.05$ , \*\* $P < 0.01$  and \*\*\* $P < 0.001$ .  $P$  values were calculated using Mann-Whitney U tests (two-sided).

and/or decreased migration into the peripheral tissues perhaps may play a role; however, this conclusion cannot be made solely based on this experiment.

Second, we performed an experiment in which the thymidine analogue 5-bromo-2'-deoxyuridine (BrdU) was injected intraperitoneally 2 h before the mice were euthanized. BrdU incorporates into newly synthesized DNA, therefore it can be used as a marker for proliferation.

Figure 4c shows that the percentage of plaque macrophages that had incorporated BrdU was not decreased by TRAF6i-HDL therapy. This result is in line with the histology observation of Ki67 expression. In an in vitro experiment with the RAW264.7 cell line of murine macrophages, which are characterized by a high proliferation rate<sup>14</sup>, incubation with the CD40-TRAF6 inhibiting compound or TRAF6i-HDL did not decrease the proliferation rate (Fig. 4d).

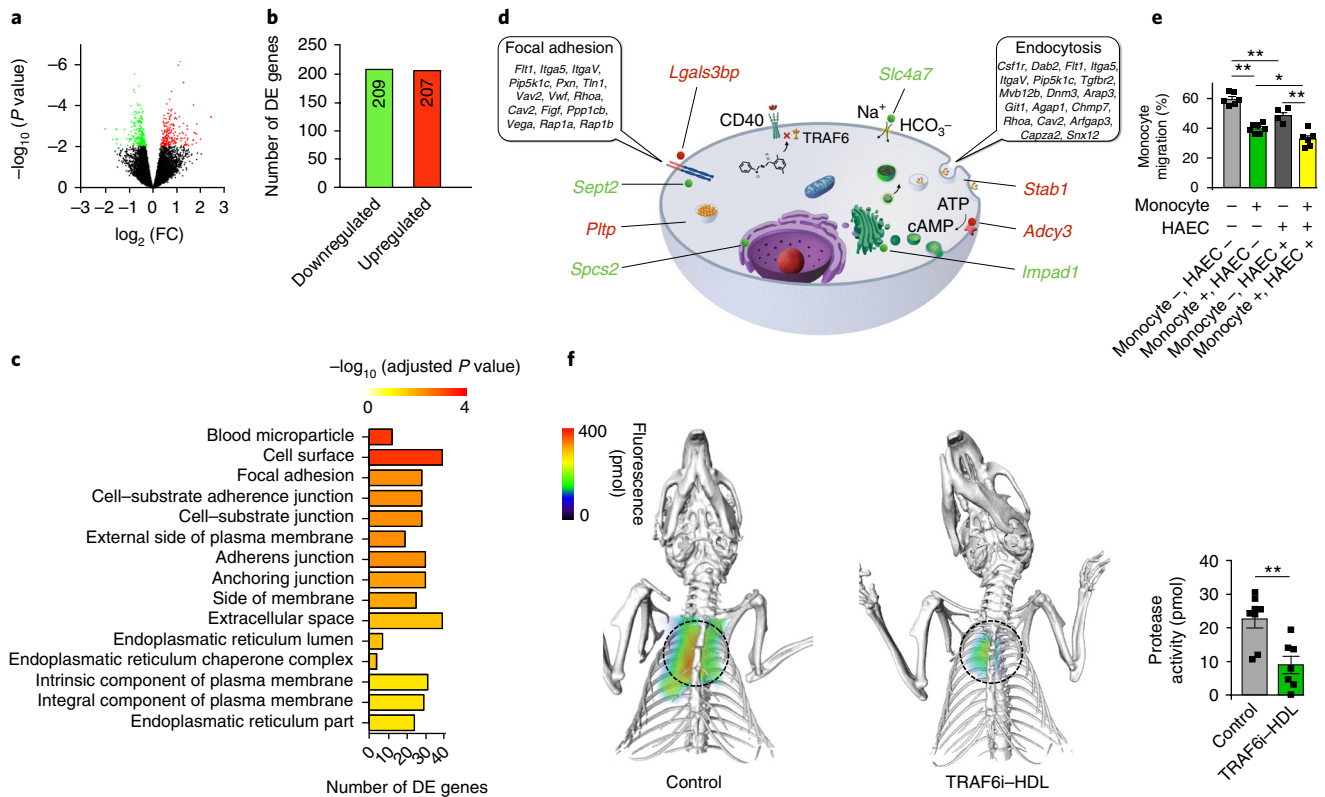


**Fig. 5 | TRAF6i-HDL shows effects on monocyte migration, among other affected processes. a–d**, Eight-week-old *Apoe*<sup>-/-</sup> mice were fed a high-cholesterol diet for 12 weeks and were then treated with four intravenous injections of either control ( $n=9$ ) or TRAF6i-HDL ( $n=9$ ) over 7 days. Twenty-four hours after the last injection, mice were euthanized, and frozen sections of aortic roots were used for the isolation of plaque macrophages by laser capture microdissection, followed by RNA isolation and sequencing for whole transcriptome analysis. **a**, Volcano plot, showing the distribution of DE genes in plaque monocytes and macrophages. DE genes between TRAF6i-HDL treatment ( $n=9$ ) and controls ( $n=9$ ) were identified using the Bioconductor package limma. The DE genes were identified by a cut-off FDR value of less than 0.2. **b**, The total number of significantly upregulated and downregulated genes according to cut-off values of an FDR threshold of 0.2. The FDR < 0.2 corresponds to a  $P < 0.009$ . **c**, Gene enrichment analysis of the DE gene set within the GO database showed 15 GO terms that were significantly enriched for DE genes (Supplementary Table 1). **d**, Schematic representation of a macrophage showing two significantly altered pathways (focal adhesion and endocytosis) identified by mapping the 416 DE genes with the KEGG pathway tool. Also depicted are the eight most significant DE genes with FDR < 0.05 and their location inside the cell (red represents upregulated, green represents downregulated; Supplementary Tables 2 and 3). **e**, In vitro transendothelial migration assay showed that TRAF6i-HDL inhibits migration of human monocytes over an endothelial barrier (HAECs).  $P$  values for control versus TRAF6i-HDL-treated monocytes are  $6.2 \times 10^{-3}$  (HAEC<sup>-</sup>) and  $1.5 \times 10^{-2}$  (HAEC<sup>+</sup>). In addition to the effect on monocytes, TRAF6i-HDL had an effect on HAECs, which may contribute to the effect on endothelial transmigration.  $P$  values for control versus TRAF6i-HDL-treated endothelial cells are  $4.5 \times 10^{-3}$  (monocytes<sup>-</sup>) and  $3.9 \times 10^{-3}$  (monocytes<sup>+</sup>);  $n=6$  per treatment condition. + indicates TRAF6i-HDL treated and - indicates control.  $P$  values were calculated using Mann-Whitney U tests (two-sided). No adjustment for multiple comparison was made. Bars represent the mean and standard error of the mean. **f**, FMT/CT imaging showed markedly decreased protease activity in the aortic root in the TRAF6i-HDL groups ( $n=7$ ) compared with the control group ( $n=8$ ;  $P=3.9 \times 10^{-3}$ ).  $P$  values were calculated using Mann-Whitney U tests (two-sided). Bars represent the mean and standard error of the mean.

Taken together, these data indicate that the plaque macrophage content was decreased by TRAF6i-HDL therapy. The mechanism by which TRAF6i-HDL decreases plaque inflammation is likely to be mediated through the abatement of monocyte recruitment, while local macrophage proliferation is unaffected.

**Mechanism of action of TRAF6i-HDL.** To gain insight into the effects of TRAF6i-HDL on the gene expression of plaque monocytes and macrophages, we isolated CD68<sup>+</sup> cells from aortic sinus plaques by laser capture microdissection of mice treated with either control or TRAF6i-HDL. Whole RNA of these cells was isolated for sequencing. We identified genes that were differentially expressed (DE) between control and TRAF6i-HDL-treated mice. Correction for multiple testing was performed with a false discovery rate (FDR) < 0.2 (Fig. 5a). A total of 416 DE genes were identified, of which 209 genes were downregulated and 207 upregulated (Fig. 5b). Gene ontology (GO) function was used to annotate the DE genes

and to find cellular components that were significantly enriched for DE genes (Fig. 5c). In the 15 enriched GO terms that were significantly enriched for DE genes, “focal adhesion” was of most interest. Other enriched GO terms, such as “cell–substrate adherent junction”, “cell–substrate junction”, “adherence junction” and “anchoring junction” are closely related to “focal adhesion”, and the genes in these GO terms overlapped to a high degree (Supplementary Table 1). Focal adhesion is a dynamic process in which protein complexes connect to the extracellular matrix and plays a central role in monocyte and macrophage migration<sup>15</sup>. In a subsequent analysis, the same 416 DE genes were mapped using the Kyoto Encyclopedia of Genes and Genomes (KEGG) pathway tool, by which we identified two significantly altered pathways, namely “focal adhesion” and “endocytosis” (Fig. 5d, Supplementary Table 2). DE genes in the focal adhesion pathway of specific interest are *Rhoa*, *Rap1a* and *Rap1b*, which play a central role in the regulation of monocyte migration by activating integrins<sup>14</sup>. These genes were all

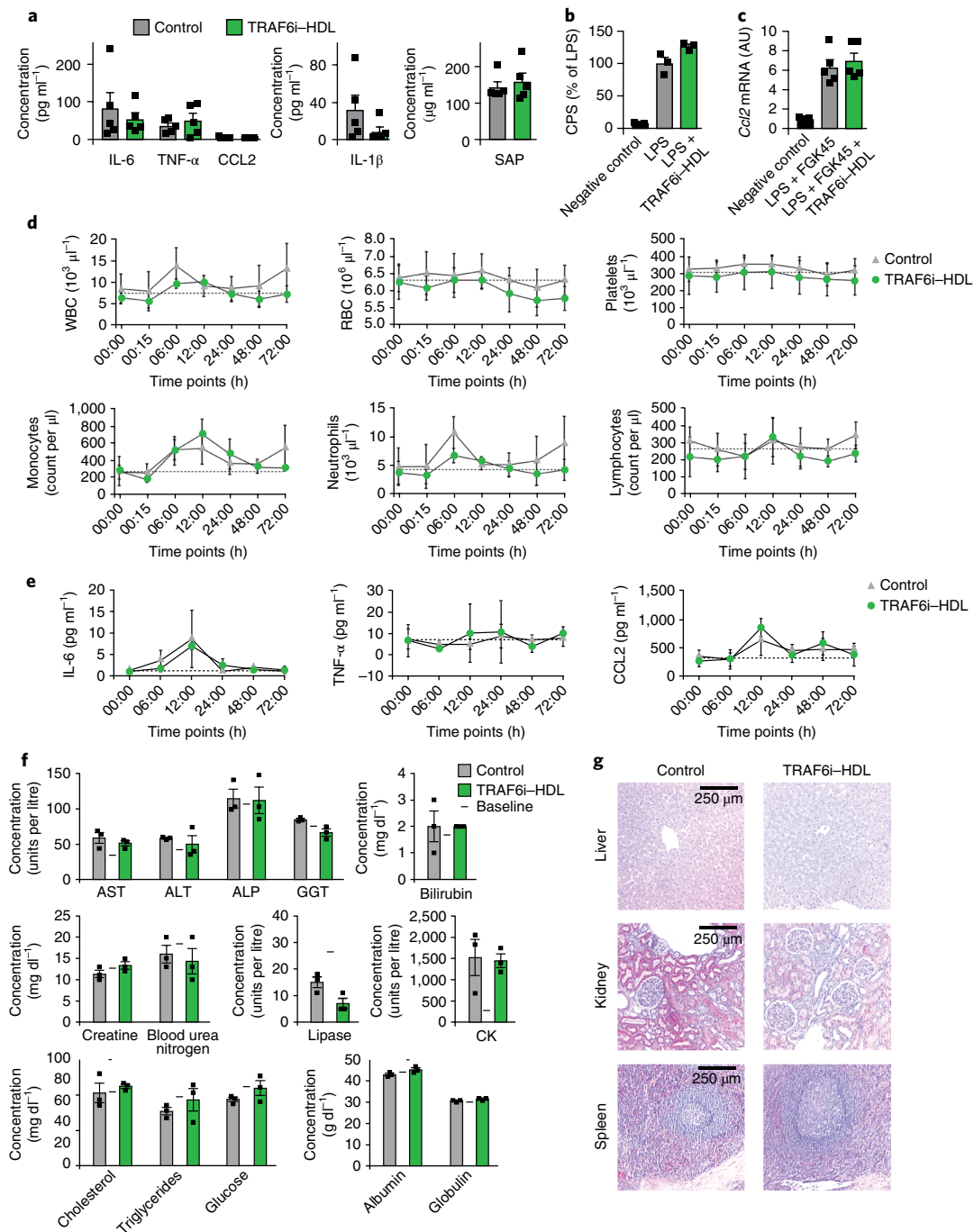


**Fig. 6 | TRAF6i-HDL therapy does not elicit adverse immune or toxic effects in mice and non-human primates.** **a**, *Apoe*<sup>-/-</sup> mice were intravenously injected with TRAF6i-HDL (5 mg kg<sup>-1</sup>) or PBS ( $n = 5$  per group). Serum was collected 24 h after injection. We found no signs of systemic immune activation. IL-6, TNF- $\alpha$ , CCL2, IL-1 $\beta$  and SAP levels were not increased. **b**, In vitro LPS stimulation test in 3x- $\kappa$ Bluc plasmid-transfected RAW264.7 cells showed that TRAF6i-HDL did not affect NF- $\kappa$ B activation. **c**, In vitro LPS and FGK45 stimulation test in bone marrow-derived macrophages showed that TRAF6i-HDL did not affect *Ccl2* expression. In **a-c**, bars represent the means and standard errors of the mean. **d-f**, Six non-human primates were infused with either control ( $n = 3$ ) or TRAF6i-HDL (1 mg kg<sup>-1</sup>;  $n = 3$ ). Blood was collected at multiple time points and the animals were euthanized 72 h after infusion. Complete blood counts showed no effects of TRAF6i-HDL therapy on lymphocytes, erythrocytes and platelets (**d**). WBC, white blood cells; RBC, red blood cells. IL-6, TNF- $\alpha$  and CCL2 were not affected by TRAF6i-HDL therapy (**e**). Means and standard deviations at each time point are shown. Extensive blood chemistry analysis showed no toxic effects of TRAF6i-HDL infusion on hepatic, renal, pancreatic or muscle cell biomarkers. Lipids, glucose, protein (albumin and globulin) and electrolytes were also unaffected (**f**). AST, aspartate aminotransferase; ALT, alanine aminotransferase; ALP, alkaline phosphatase; GGT, gamma-glutamyl transferase; CK, creatine kinase. Bars represent the means and standard deviations. **g**, Specimens from liver, kidneys and spleen were sectioned and stained (H&E) for histological analysis and evaluated by a pathologist ( $\times 10$  magnification is shown). No signs of tissue damage or disturbances in tissue architecture were found in any of the tissues (single experiment). For all figures,  $P$  values were calculated using Mann-Whitney U tests (two sided).

significantly downregulated. One of the most highly upregulated DE genes (FDR < 0.05) was *Stab1* (which encodes stabilin 1); this gene is associated with an atheroprotective macrophage phenotype and is known to have functions in lymphocyte homing and cell adhesion<sup>16,17</sup>. Other highly significant DE genes (FDR < 0.05) were identified that are not known to be related to monocyte migration (Fig. 5d, Supplementary Table 3). We did not observe an effect on gene expression related to macrophage proliferation, apoptosis, migratory egress, macrophage polarization or monocyte-to-macrophage differentiation (Supplementary Table 4). These data are in line with our *in vivo* observations of decreased Ly6C<sup>hi</sup> monocyte recruitment in TRAF6i-HDL-treated *ApoE*<sup>-/-</sup> mice.

To corroborate the transcriptome analysis data, we functionally examined adhesive and migratory capacity via an *in vitro* transendothelial migration assay using tissue necrosis factor- $\alpha$  (TNF- $\alpha$ )-stimulated human arterial endothelial cells (HAECs) and monocytes. We observed that when monocytes were pretreated with TRAF6i-HDL, the transendothelial migration of monocytes was markedly decreased (Fig. 5e, Supplementary Fig. 7, Supplementary Video 3). This result confirms our finding from the whole transcriptome analysis. An additional beneficial effect of TRAF6i-HDL may be mediated through effects on endothelial cells. When TNF- $\alpha$ -stimulated HAECs were treated, decreased transendothelial migration of untreated monocytes was observed. The strongest decrease in transendothelial migration was observed when both HAECs and monocytes were treated (Fig. 5e). Altogether, these data show that decreased monocyte infiltration in the plaque is an important mechanism by which TRAF6i-HDL exerts its effect on plaque inflammation, and may be mediated by the effect of TRAF6i-HDL on monocyte migratory capacity as well as by effects on the endothelium.

To ultimately establish that the decreased numbers of monocytes and macrophages in the plaque resulted in decreased plaque inflammation, we performed fluorescence molecular tomography (FMT) fused with CT imaging to visualize protease activity in the aortic sinus area. Control-treated ( $n = 8$ ) and TRAF6i-HDL-treated ( $n = 7$ ) *ApoE*<sup>-/-</sup> mice all received a single injection of an activatable pan-cathepsin protease sensor 24 h before imaging. The protease sensor is taken up by activated macrophages, followed by cleavage of the protease sensor within the endolysosome, yielding fluorescence as a function of enzyme activity. TRAF6i-HDL therapy decreased protease activity by 60% ( $P = 0.002$ , Fig. 5f).

**Toxicity and effects of TRAF6i-HDL on the immune system in atherosclerotic mice and non-human primates.** In atherosclerotic mice, 1 week of TRAF6i-HDL treatment had no effect on erythrocytes, platelets or leukocyte levels (Supplementary Table 5). The number of reticulocytes was increased in both the reconstituted high-density lipoprotein (rHDL) and TRAF6i-HDL groups compared with the control group. This increase was apparently not caused by SMI 6877002. ApoA-I is not known to have an effect on erythropoiesis. The number of erythrocytes was unchanged and we did not observe signs of red cell destruction. The numbers of T cells and B cells in bone marrow, blood and spleen were not affected by TRAF6i-HDL therapy (Supplementary Fig. 5a,b). No toxic effects were observed on kidney and hepatic function, although alkaline phosphatase was increased (Supplementary Table 6). Lipid, glucose, protein and electrolyte levels were unaffected.

Subsequently, we investigated the potential adverse immune effects of TRAF6i-HDL on evoking or suppressing systemic inflammatory responses by measuring serum cytokines and chemokines. IL-6, IL-1 $\beta$ , chemokine (C-C motif) ligand 2 (CCL2), TNF- $\alpha$  and serum amyloid P-component (SAP) levels were unaffected (Fig. 6a).

Next, we investigated whether CD40-TRAF6 inhibition affects the response of macrophages (RAW264.7 cells) to lipopolysaccharide (LPS) stimulus *in vitro*. We found that LPS-induced nuclear

factor- $\kappa$ B (NF- $\kappa$ B) activation is not inhibited by CD40-TRAF6 blockade (Fig. 6b). This observation was reproduced in bone marrow-derived macrophages (BMDMs) from C57BL/6 mice, which were stimulated with LPS and the agonistic CD40 antibody FGK45 (Fig. 6c). RNA was isolated from BMDMs to assess *Ccl2* expression as a marker for macrophage activation. Incubation with TRAF6i-HDL did not affect *Ccl2* RNA expression. Altogether, these data indicate that our nanoimmunotherapy has a favourable immunological safety profile. Notably, the bare CD40-TRAF6 inhibiting compound was previously investigated in a sepsis model, and no signs of an incompetent immune response were found. In fact, survival was improved<sup>8</sup>.

To assess the translatability of TRAF6i-HDL therapy in non-human primates, we performed comprehensive blood testing and histological analyses. Six non-human primates were used for complete haematological, post mortem histological and blood chemistry analyses. The non-human primates were injected with either control or a single dose of TRAF6i-HDL (1 mg kg<sup>-1</sup>) and euthanized after 72 h.

Complete blood count data from 7 time points within 72 h after injection showed no differences between control-treated and TRAF6i-HDL-treated animals in white blood cells, monocytes, neutrophils, lymphocytes, red blood cells, platelets or any of the other indices (Fig. 6d, Supplementary Fig. 8a). Furthermore, TRAF6i-HDL did not affect IL-6, TNF- $\alpha$  and CCL2 indicating that it neither evokes nor suppresses systemic inflammatory responses (Fig. 6e).

Since the major accumulation site of the nanoparticles is in the liver, it is paramount to assess whether our therapy had toxic effects on this organ. Based on what is known from previous studies, we would not expect liver toxicity from CD40-TRAF6 inhibition. Under physiological conditions, CD40 expression by hepatocytes is negligible. Therefore, CD40-TRAF6 inhibition is unlikely to affect hepatocytes<sup>18</sup>. Under pathological conditions, hepatocytes express CD40, which renders stimulation of CD40 signalling harmful<sup>19,20</sup>. Our nanoimmunotherapy does the opposite and — under pathological conditions — may therefore exert a therapeutic benefit. Indeed, the blood chemistry analysis confirmed that TRAF6i-HDL had no toxic effect on the liver (Fig. 6f). This result was corroborated by liver histology (H&E), which showed no signs of tissue damage or disturbances in tissue architecture (Fig. 6g).

Additionally, the blood chemistry analysis showed no signs of renal, pancreatic or muscle cell toxicity in the TRAF6i-HDL-treated group compared with the control group (Fig. 6f). Furthermore, lipid, glucose and protein (albumin and globulin) levels were equal in both groups (Fig. 6e, Supplementary Fig. 8b). Electrolytes were also unaffected (Supplementary Fig. 8b). Kidney and spleen histology (H&E) showed no signs of tissue damage or disturbances in tissue architecture (Fig. 6g).

## Discussion

We have described the development and evaluation of a HDL-based nanoimmunotherapy (TRAF6i-HDL) that modulates the CD40-TRAF6 interaction in monocytes and macrophages. Our data showed that TRAF6i-HDL has a strong affinity for monocytes and macrophages in the haematopoietic organs, blood and atherosclerotic lesions. A week of therapy rapidly reduced plaque macrophage content, which can partly be attributed to the inhibition of monocyte recruitment that is mediated through impairment of the monocyte migratory capacity and potential additional effects on the endothelium. TRAF6i-HDL also proved to be safe in non-human primates, thus supporting the translational potential of this therapy.

Taking a multiparametric approach, we not only teased out the therapeutic potential of TRAF6i-HDL but also highlighted the significance of integrating advanced *in vivo* imaging techniques to study its *in vivo* behaviour. In particular, the PET/MRI data

acquired in non-human primates provided compelling information about the distribution kinetics of TRAF6i–HDL in a species closely related to humans.

The CD40–CD40L signalling axis has long been recognized to play an imperative role in eliciting immune responses in atherosclerosis<sup>2–5</sup>. While its identification gave rise to high anticipation, therapeutic targeting of this co-stimulatory receptor–ligand pair proved cumbersome. An anti-CD40L antibody was effective in diminishing atherosclerosis development in mice<sup>3–5</sup>, but thromboembolic complications due to CD40 expression on platelets prohibited its application in humans<sup>21,22</sup>. Furthermore, CD40 is expressed on B lymphocytes, and prolonged blockade would impair their maturation, causing immunodeficiency<sup>23</sup>. In the current study, we addressed these issues by targeting the interaction between TRAF6 and the cytoplasmic domain of CD40 in monocytes and macrophages. We achieved this goal by using HDL as a nanocarrier for a small-molecule inhibitor of the CD40–TRAF6 interaction. Our data showed that our HDL-based nanoimmunotherapy exposed over 80% of monocytes and macrophages to its cargo, while lymphocytes did not take up any nanoparticles. These observations corroborate our previous work on the targeting efficiency of HDL-based drug delivery<sup>24</sup>.

We also aimed to minimize drug exposure by using a short duration of therapy (1 week). Previous therapeutic studies targeting the CD40–CD40L signalling axis used prolonged treatment times<sup>3–5</sup>. We found a 49% and 66% decrease in plaque Ly6C<sup>hi</sup> monocyte and macrophage content, respectively, within 1 week, thus signifying the high potency of TRAF6i–HDL nanoimmunotherapy. Of note, we proved that apoA-I provides only a minor contribution to the therapeutic effect of TRAF6i–HDL. We used four infusions of 9 mg kg<sup>-1</sup> apoA-I, which is relatively low compared with those used in previously published studies<sup>25</sup>, and we found no effects of empty HDL on plaque monocyte or macrophage content compared with controls.

The mechanism by which TRAF6i–HDL decreased plaque inflammation on such a short timescale can in part be explained by decreased monocyte recruitment. In general, plaque macrophage content is determined by a balance of monocyte recruitment and macrophage proliferation, apoptosis and migratory egress. The first two processes are considered the most important determinants<sup>10,26–28</sup>. Our data did not reveal an effect on macrophage proliferation, apoptosis or migratory egress. We did, however, observe a decrease in plaque Ly6C<sup>hi</sup> monocyte content while the blood monocyte count was unaffected, indicative of decreased monocyte recruitment. This result is in line with previous observations in a knockout mouse model with defective CD40–TRAF6 signalling. In a previous study, *CD40-T6*<sup>-/-</sup> mice were used to investigate the migratory capacity of monocytes and macrophages<sup>7</sup>. By performing in vivo intravital microscopy, it was shown that Ly6C<sup>hi</sup> monocytes displayed impaired luminal adhesion to the wall of carotid arteries. Furthermore, *CD40*<sup>-/-</sup> as well as *CD40-T6*<sup>-/-</sup> macrophages displayed an impaired migration towards CCL2 in an in vitro Transwell migration assay<sup>7</sup>. In the current study, the comparative whole transcriptome analysis and in vitro monocyte migration assays confirmed that CD40–TRAF6 inhibition affects monocyte recruitment. We observed a differential expression of genes involved in focal adhesion. *Rhoa*, *Rap1a* and *Rap1b*, which are involved in activating integrins, were among the genes that were significantly downregulated. Although the differential gene expression was investigated in plaque monocytes and macrophages, we deem it likely that TRAF6i–HDL affects myeloid cells systemically. We observed nanoparticle uptake by myeloid cells in the haematopoietic organs, and TRAF6i–HDL treatment increased Ly6C<sup>hi</sup> monocytes in the bone marrow, blood and spleen. Why Ly6C<sup>hi</sup> monocytes were increased in these tissues was not investigated, but may be related to either an increased production or decreased mobilization of these cells.

In addition to treatment effects on monocyte and macrophages, TRAF6i–HDL may have an effect on the endothelium. Monocyte infiltration into atherosclerotic lesions involves a close dialogue between monocytes and the endothelium. Activated endothelial cells express adhesion molecules that interact with glycosylated ligands and integrins expressed by monocytes. Although we did not investigate the uptake of TRAF6i–HDL by endothelial cells in vivo, we did observe in an in vitro assay that TRAF6i–HDL inhibits monocyte transmigration through the endothelium. This result suggests that beneficial effects of TRAF6i–HDL on the endothelium may contribute to the observed decrease in monocyte recruitment.

Our data showed high monocyte kinetics in atherosclerosis, which corroborates observations reported in previous studies<sup>1,12,26–28</sup>. In fact, decreased recruitment was shown to cause over 70% reduction in plaque macrophage content within 4 weeks<sup>27</sup>. Vice versa, a sudden increase in monocyte recruitment, induced by myocardial infarction, caused a marked increase in plaque macrophage content within 1–3 weeks<sup>28</sup>. These observations are in line with our findings of decreased monocyte recruitment causing a 66% decrease of plaque macrophage content within 1 week.

Regarding the translatability of our therapy, we performed extensive pharmacokinetic, biodistribution and safety experiments in non-human primates. The use of reconstituted HDL has previously been proven to be safe in humans given apoA-I of 40 mg kg<sup>-1</sup> doses<sup>29,30</sup>. The amount of apoA-I used in our formulation, 1.8 mg kg<sup>-1</sup>, therefore poses no safety issues. Scaling up the production to a magnitude that would suffice for application in humans is feasible. Adequate amounts of apoA-I can be obtained from human plasma (native apoA-I), bacteria or transgenic plants (recombinant apoA-I) or synthetically<sup>31–34</sup>. These methods have been applied in large clinical trials in humans<sup>34–36</sup>. Scaling the reconstitution of drug-loaded HDL nanoparticles can be done with high-pressure homogenization-based approaches or microfluidics<sup>37</sup>.

The small-molecule inhibitor of the CD40–TRAF6 interaction that was recently developed has not yet been evaluated in humans. The biodistribution of <sup>89</sup>Zr-labelled TRAF6i–HDL was consistent with our previous observations of <sup>89</sup>Zr-labelled HDL in murine, rabbit and porcine atherosclerosis models<sup>38</sup>. We observed the highest accumulation in the liver, spleen and kidneys. The liver and kidneys are the main sites of apoA-I and HDL catabolism, and the spleen is the major secondary lymphoid organ containing many myeloid cells that clear the nanoparticles from the circulation. There were no signs of toxic effects in the liver, kidney or spleen, and all tissues showed normal tissue architecture on histological analyses. Furthermore, the complete blood count did not show any effects on the numbers of platelets, lymphocytes, monocytes, neutrophils or red blood cells. Safety data were assessed up until 72 h post administration. Long-term safety was not addressed in the current study.

Until recently, no therapies were evaluated that are specifically aimed at reducing vascular inflammation. Statins are known to have beneficial cardiovascular effects beyond cholesterol lowering<sup>39</sup>. Currently, chronic therapy with low-dose methotrexate is being investigated in a large Phase III clinical trial<sup>40</sup>. A recently published Phase III clinical trial showed that chronic therapy with an IL-1 $\beta$  monoclonal antibody decreased the cardiovascular event rate<sup>41</sup>. This trial provides clinical evidence that immunotherapy can be beneficially applied in cardiovascular disease. The effect of chronic IL-1 $\beta$  antibody therapy was, however, modest, with a 2% absolute risk reduction in the primary endpoint and came at the cost of a higher incidence of fatal infection. We specifically designed our nanoimmunotherapy to rapidly suppress plaque inflammation in patients at high risk of cardiovascular events. While targeted delivery enhances efficacy, its short-term application minimizes the risks associated with prolonged immunosuppression. Patients admitted for an acute coronary syndrome may be an appropriate population for such induction therapy of inflammation since they have a

markedly increased risk of recurrent myocardial infarction of up to 17.4% within the first year<sup>42</sup>. Recent studies have proposed that it is the initial myocardial infarction itself that evokes monocyte recruitment to atherosclerotic plaques, causing them to become inflamed and vulnerable for plaque rupture<sup>28</sup>. In this pathophysiological context, our concept of rapid suppression of monocyte recruitment in the vulnerable phase might be relevant.

In summary, this study described a rapid induction therapy to treat inflammation in atherosclerosis, whereby CD40–TRAF6 signalling in monocytes and macrophages is modulated. Our infusible HDL-based nanoimmunotherapy has potential for clinical translation, as attested by the favourable safety data in non-human primates.

## Methods

**Synthesis and characteristics of TRAF6i–HDL.** The synthesis of TRAF6i–HDL was based on a previously published method<sup>34,43</sup>. In short, the CD40–TRAF6 inhibitor SMI 6877002<sup>8</sup> was combined with MHPC and DMPC (Avanti Polar Lipids) in a chloroform–methanol mixture (9:1 by volume) and then dried in a vacuum, yielding a thin lipid film. A PBS solution of human apoA-I was added to the lipid film. The mixture was incubated at 37°C for 1 h or until the film was hydrated and a homogenous solution was formed. The solution was then sonicated for 20 min to form TRAF6i–HDL nanoparticles. Subsequently, the solution was purified by multiple centrifugal filtration steps. For targeting, imaging and biodistribution experiments, analogues of TRAF6i–HDL were prepared through incorporation of the fluorescent dyes DiR or DiO (Invitrogen) in the core, or the phospholipid chelator DSPE-DF0 (1 mol % at the expense of DMPC), which enables radiolabelling with <sup>89</sup>Zr<sup>44</sup>.

TRAF6i–HDL was characterized using a combination of dynamic light scattering, transmission electron microscopy and size exclusion chromatography (SEC). In addition, the zeta potential was determined. Size was evaluated as function of time at 4°C by dynamic light scattering and SEC. Drug release was measured by a dialysis method at 4°C and 37°C in PBS, as well as in fetal bovine serum at 37°C. Finally, <sup>89</sup>Zr labelling stability was established by SEC.

**Animals and diet for the mouse studies.** Female *ApoE*<sup>-/-</sup> mice (B6.129P2-Apoetm1Unc, *n* = 103) were used for this study. All animal care and procedures were based on an approved institutional protocol from the Icahn School of Medicine at Mount Sinai. Eight-week-old *ApoE*<sup>-/-</sup> mice were purchased from The Jackson Laboratory. All mice were fed a high-cholesterol diet (0.2% weight cholesterol; 15.2% kcal protein, 42.7% kcal carbohydrate, 42.0% kcal fat; Harlan TD. 88137) for 12 weeks.

The treatment protocol in each experiment was identical and was as follows: 20-week-old *ApoE*<sup>-/-</sup> mice were randomly assigned to either control (PBS infused in the same volume as in the other groups), empty rHDL or TRAF6i–HDL (5 mg kg<sup>-1</sup>) groups. Mice were treated with four intravenous injections over 7 days, while kept on a high-cholesterol diet during treatment. Animals were euthanized 24 h after the last injection.

**Flow cytometry.** *ApoE*<sup>-/-</sup> mice were euthanized and perfused with PBS, after which the aorta from the aortic root to the iliac bifurcation was gently cleaned from fat and collected. Whole aortas were put in an enzymatic digestion solution containing liberase TH (4 U ml<sup>-1</sup>) (Roche), deoxyribonuclease (DNase) I (40 U ml<sup>-1</sup>) (Sigma-Aldrich) and hyaluronidase (60 U ml<sup>-1</sup>) (Sigma-Aldrich), minced and placed in a 37°C incubator for 60 min. Cells were filtered through a 70 µm strainer, and twice spun down and resuspended in serum-containing media. Spleens were weighed and filtered through a 70 µm cell strainer, spun down, resuspended in red cell lysis buffer for 4 min, and then inactivated using serum-containing media, spun down and resuspended in 1,000 µl serum-containing media per 100 mg of spleen tissue. EDTA-treated blood was spun down, resuspended in red cell lysis buffer for 4 min, and then inactivated using serum-containing media, spun down and resuspended in 100 µl of serum-containing media. Bone marrow was obtained from a single femur. The intact femurs were rinsed with 70% ethanol followed by three subsequent washes in ice-cold sterile PBS. The epiphyses were cut off, and the bone marrow was flushed out with PBS. Cells were filtered through a 70 µm strainer, spun down and resuspended in red cell lysis buffer for 30 s, and then inactivated using serum-containing media, spun down and resuspended in 1,000 µl of serum-containing media. The following antibodies were used: F4/80-PE-Cy7 (clone BM8, BioLegend); CD11b-PerCP/Cy5.5 (clone M1/70, BioLegend); CD11c-APC (clone N418, BioLegend); CD45-brilliant violet 510 (clone 30-F11, BioLegend); Ly6C-PE (clone AL-21, BD Biosciences); Ly6C-FITC (clone AL-21, BD Biosciences); CD90.2-eFluor 450 (clone 53-2.1, eBioscience); CD90.2-PE (clone 53-2.1, BD Biosciences); Ter119-eFluor 450 (clone TER-119, eBioscience); NK1.1-eFluor 450 (clone PK136, eBioscience); NK1.1-PE (clone PK136, BD Biosciences); CD49b-eFluor 450 (clone DX5, eBioscience); CD45R-eFluor450 (clone RA3-6B2, eBioscience);

Ly-6G-Pacific Blue (clone 1A8, BioLegend); Ly-6G-PE (clone 1A8, BD Biosciences); CD3-PE (clone 17A2; BioLegend); and CD19-PE (clone 1D3, BD Biosciences). The antibody dilutions ranged from 1:200 to 1:100. The contribution of newly made cells to different populations was determined by in vivo labelling with BrdU. Incorporation was measured using allophycocyanin (APC)-conjugated anti-BrdU antibodies according to the manufacturer's protocol (BD APC-BrdU Kit, 552598). Monocytes and macrophages were identified using a method similar to a previously described method<sup>10–12</sup>. Specifically, Ly6C<sup>hi</sup> monocytes were identified as CD11b<sup>hi</sup>, CD11c<sup>low</sup>, Lin<sup>-low</sup> (with Lin defined as CD90.2<sup>+</sup>, CD45R<sup>+</sup>, CD49b<sup>+</sup>, NK1.1<sup>+</sup>, Ly-6G<sup>+</sup>, Ter119<sup>+</sup> or CD90.2<sup>+</sup>, NK1.1<sup>+</sup>, Ly-6G<sup>+</sup>, CD19<sup>+</sup>, CD3<sup>+</sup>) F4/80<sup>low</sup> that were also Ly6C<sup>hi</sup>. Macrophages were identified as CD11b<sup>hi</sup>, CD11c<sup>low</sup>, Lin<sup>-low</sup>, F4/80<sup>hi</sup>, CD11<sup>-low</sup>. Data were acquired on an LSRII flow cytometer (BD Biosciences) and analysed using FlowJo v10.0.7 (Tree Star).

**Histology and immunohistochemistry.** Tissues for histological analyses were collected and fixed overnight in formalin and embedded in paraffin. Aortic roots were sectioned into 4 µm slices, generating a total of 90–100 cross-sections per root. Eight cross-sections were stained with H&E and used for atherosclerotic plaque size measurement. Other sections were deparaffinized, blocked, incubated in 95°C antigen-retrieval solution (DAKO), and immunolabelled with either anti-Mac3 rat monoclonal antibody (1:30; BD Biosciences) or anti-Ki67 rabbit polyclonal antibody (1:200, Abcam). Sirius Red staining was used for analysis of collagen content. Antibody staining was visualized by either ImmPact AMEC red (Vectorlabs) or diaminobenzidine (DAB). Sections were analysed using a Leica DM6000 microscope (Leica Microsystems) or a VENTANA iScan HT slide scanner (Ventana).

**Laser capture microdissection and RNA sequencing.** Laser capture microdissection was performed on 24 aortic root sections (6 µm) as previously described<sup>19</sup>. In short, frozen sections were dehydrated in graded ethanol solutions (70% twice, 95% twice, 100% once), washed with diethyl pyrocarbonate (DEPC)-treated water, stained with Mayer's H&E and cleared in xylene. For every 8 sections, 1 section was used for CD68 staining (Abdsrotec, 1:250 dilution), which was used to guide the laser capture microdissection. CD68-rich areas within the plaques were identified and cut out using a ArcturusXT LCM System. The collected CD68<sup>+</sup> cells were used for RNA isolation (PicoPure RNA Isolation Kit, Arcturus) and subsequent RNA amplification and cDNA preparation according to the manufacturers protocols (Ovation Pico WTA System, NuGEN). The quality and concentration of the collected samples were measured using an Agilent 2100 Bioanalyzer. For RNA sequencing, pair-end libraries were prepared and validated. The purity, fragment size, yield and concentration were determined. During cluster generation, the library molecules were hybridized onto an Illumina flow cell. Subsequently, the hybridized molecules were amplified using bridge amplification, resulting in a heterogeneous population of clusters. The dataset was obtained using an Illumina HiSeq 2500 sequencer.

**Differential expression and function annotation analysis.** The pair-ended sequencing reads were aligned to human genome hg19 using tophat aligner (bowtie2)<sup>45</sup>. Following the read alignment, HTSeq<sup>46</sup> was used to quantify gene expression at the gene level based on GENCODE gene model release 22<sup>47</sup>. Gene expression raw read counts were normalized as counts per million using trimmed mean of M-values normalization method to adjust for the sequencing library size difference among samples. DE genes between drug treatments and controls were identified using the Bioconductor package limma<sup>48</sup>. To correct for the multiple testing problem, limma was used to calculate statistics and *P* values in random samples after a permutation of labels. This procedure was repeated 1,000 times to obtain null *t*-statistic and *P* value distribution for estimating FDR values of all genes. The DE genes were identified using a cut-off of corrected *P* value of less than 0.2. GO function<sup>49</sup> was used to annotate the DE genes and to find cellular components that were significantly enriched for the DE genes. DE genes were also mapped to the KEGG pathway using KEGG Mapper<sup>50</sup>.

**FMT/CT imaging.** Female *ApoE*<sup>-/-</sup> mice fed a high-cholesterol diet for 12 weeks were treated with either four TRAF6i–HDL infusions (5 mg kg<sup>-1</sup>, *n* = 7) or saline (*n* = 8) over 7 days. Five nanomoles of pan-cathepsin protease sensor (ProSense 680, PerkinElmer, Cat no. NEV10003) was intravenously administered 24 h before imaging. For the FMT/CT imaging, animals were placed in a custom-built imaging cartridge, which was equipped for isoflurane administration during imaging. Animals were first scanned using a high-resolution CT scanner (Inveon PET-CT, Siemens), with a continuous infusion of CT-contrast agent (isovue-370, Bracco Diagnostics) at a rate of 55 µl min<sup>-1</sup> through a tail vein catheter. Animals were subsequently scanned using an FMT scanner (PerkinElmer) in the same cartridge. The CT X-ray source with an exposure time of 370–400 ms was operated at 80 kVp and 500 mA. Contrast-enhanced high-resolution CT images were used to localize the aortic root, which was used to guide the placement of the volume of interest for the quantitative FMT protease activity map. Image fusion relied on fiducial markers. Image fusion and analysis was performed using OsiriX v.6.5.2 (The OsiriX Foundation, Geneva).

**LPS stimulation test in RAW264.7 cells.** RAW264.7 cells, stably transfected with the 3 $\times$ - $\kappa$ Bluc plasmid<sup>9</sup>, were incubated with the small molecules (10  $\mu$ M) or vehicle for 1 h. Subsequently, cells were activated using LPS from *Escherichia coli* (Sigma-Aldrich). After 2 h, cells were lysed, and substrate was added according to the manufacturer's protocol (Luc-screen system; Applied Biosystems). Emission was measured at 450 nm using a Wallac Victor II luminometer.

**In vitro LPS and FGK45 stimulation test in BMDMs.** Bone marrow cells were isolated from C57BL/6 mice, and cultured in RPMI supplemented with 15% L929-conditioned medium to generate BMDMs. One hour before activation, BMDMs were incubated with TRAF6i-HDL (10  $\mu$ M). BMDMs were activated by the agonistic CD40 antibody FGK45 (30  $\mu$ g ml<sup>-1</sup>, Bioceros BV) and LPS (1 ng ml<sup>-1</sup>, Sigma) for 6 h. RNA was isolated from BMDMs and reverse transcribed using an iScript cDNA synthesis kit (Bio-Rad). Quantitative PCR was performed using a SYBR Green PCR kit (Applied Biosystems) on a ViiA 7 real-time PCR system (Applied Biosystems). Primer sequences are available upon request.

**Radiolabelling of HDL nanoparticles.** Ready-to-label HDL nanoparticles were prepared by including 1 mol% the phospholipid-chelator DSPE-DF0 in the formulation mix at the expense of DMPC. The DFO-containing nanoparticles were then labelled with <sup>89</sup>Zr as previously described<sup>38</sup>. Briefly, the nanoparticles were reacted with <sup>89</sup>Zr-oxalate in PBS (pH 7.1) at 37 °C for 1 h. Purification was carried out by centrifugal filtration using 10 kDa molecular weight cut-off filter tubes and washing twice with fresh sterile PBS. The radiochemical yield was 90  $\pm$  4% ( $n$  = 3) and the radiochemical purity was >97%, as determined by SEC.

**Pharmacokinetics, biodistribution and PET/CT imaging studies in mice.** Female *ApoE*<sup>-/-</sup> mice fed a high-cholesterol diet for 12 weeks ( $n$  = 4, 25.5  $\pm$  2.6 g body weight) were injected with <sup>89</sup>Zr-TRAF6i-HDL nanoparticles (183  $\pm$  16  $\mu$ Ci, 5 mg TRAF6i-HDL per kg). At predetermined time points (2, 15 and 30 min, and 1, 4, 8 and 24 h) blood samples were taken, weighed and measured for radioactivity content using a 2470 Wizard automatic gamma counter (Perkin Elmer). Data were converted to %ID g<sup>-1</sup>, plotted in a time-activity curve and fitted using a non-linear two-phase decay regression in Prism GraphPad (GraphPad Software inc, USA). A weighted blood radioactivity  $t_{1/2}$  was finally calculated.

Twenty-four hours after injection, the animals were scanned on an Inveon PET/CT scanner (Siemens Healthcare Global) under a isoflurane/oxygen gas mixture (2% for induction, 1% for maintenance) for anaesthesia. The PET static scan recorded a minimum of 25 million coincident events and lasted 10 min. The energy and coincidence timing windows were 350–700 keV and 6 ns, respectively. Image data were normalized to correct for nonuniformity of response of the PET, dead-time count losses, positron branching ratio, and physical decay to the time of injection, but no attenuation, scatter or partial-volume averaging correction was applied. The counting rates in the reconstructed images were converted to activity concentrations (%ID g<sup>-1</sup>) by using a system calibration factor derived from the imaging of a mouse-sized water-equivalent phantom containing <sup>89</sup>Zr. Images were analysed using ASIPro VMTM (Concorde Microsystems) and Inveon Research software (Siemens Healthcare Global). Quantification of activity concentration was performed by averaging the maximum values in at least five regions of interest (ROIs) drawn on adjacent slices of the tissue of interest. Whole-body standard low-magnification CT scans were performed with the X-ray tube setup at a voltage of 80 kV and current of 500  $\mu$ A. The CT scan was acquired using 120 rotational steps for a total of 220 degrees yielding and estimated scan time of 120 s with an exposure of 145 ms per frame. Immediately after the PET/CT scan, animals were euthanized and perfused with PBS. Tissues of interest (liver, kidneys, spleen, lungs, muscle, heart, aorta, bone and brain) were collected, blotted and weighed. Radioactivity was measured by gamma counting, and the radioactivity concentration was expressed as %ID g<sup>-1</sup>.

**Autoradiography.** Following radioactivity counting, aortas were placed in a film cassette against a phosphorimaging plate (BASMS-2325, Fujifilm) for 24 h at -20 °C to determine the radioactivity distribution. The plates were read at a pixel resolution of 25  $\mu$ m with a Typhoon 7000IP plate reader (GE Healthcare).

**Ex vivo NIRF.** Female *ApoE*<sup>-/-</sup> mice fed a high-cholesterol diet for 12 weeks received a single intravenous injection of DiR (0.5 mg kg<sup>-1</sup>)-labelled TRAF6i-HDL (5 mg kg<sup>-1</sup>,  $n$  = 2) or saline ( $n$  = 1). Mice were euthanized 24 h after the injection and perfused with 60 ml PBS. Liver, spleen, lung, kidneys, heart and muscle tissue were collected for NIRF imaging. Fluorescent images were acquired using a IVIS 200 system (Xenogen), with a 2 s exposure time, a 745 nm excitation filter and an 820 nm emission filter. ROIs were drawn on each tissue with software provided by the vendor, after which quantitative analyses were performed using the average radiant efficiency within these ROIs.

**Blood tests in mice.** Blood was collected by heart puncture at the time of death. Serum was sent to IDEXX Laboratories (Totowa) and analysed using an Olympus AU400 Chemistry Analyzer. Whole blood was collected in EDTA-containing tubes and analysed using an IDEXX procyte DX Hematology Analyzer for complete blood count analysis.

For the multiplex analysis, mice were intravenously injected with TRAF6i-HDL at 5 mg kg<sup>-1</sup> or with PBS. Serum was collected 24 h after injection. Levels of IL-6, TNF- $\alpha$ , CCL2, IL-1 $\beta$  and SAP were measured using the Milliplex detection kits MAP2MAG-76K and MCYTOMAG-70k (Millipore Corporation). Samples were run in triplicate.

**In vitro transendothelial monocyte migration assay.** HAECs (purchased from Lonza) were cultured to confluency and subsequently stimulated with TNF- $\alpha$  (10 ng ml<sup>-1</sup>) overnight. HAECs were either pre-incubated for 30 min with 35  $\mu$ M of CD40-TRAF6 inhibitor or dimethylsulfoxide as the solvent control. Subsequently, the culture medium containing the compound was replaced by regular EMG-2 medium, and the transendothelial migration assay was performed 20 min later. The assay was performed with monocytes pretreated for 30 min with either 35  $\mu$ M of CD40-TRAF6 inhibitor or dimethylsulfoxide as the solvent control. Pretreatment was performed under shaking conditions in polypropylene, low-retention tubes (Falcon, Corning) to minimize adhesion during the incubation step. Monocytes were added at a temperature of 37 °C, 5% CO<sub>2</sub> and then fixed with 3.7% formaldehyde 30 min after addition (Sigma-Aldrich). Multiple images were recorded per well using a Leica DMi8 microscope (Plan-Apochromat  $\times$  10/0.25 Phaco 1 objective; Leica). Adhered (bright morphology) and transmigrated monocytes (dark morphology) were quantified using the cell counter plugin (<http://rsbweb.nih.gov/ij/plugins/cell-counter.html>) in Image-J software (<http://rsb.info.nih.gov/nih-image/>) version 2.00-rc-43.

**Non-human primate studies.** Adult male cynomolgus monkeys (*Macaca fascicularis*) were used for the non-human primate studies, which were conducted at the University of Kentucky and the Icahn School of Medicine at Mount Sinai. The average weight of the animals was 7.3  $\pm$  1.98 kg (mean  $\pm$  S.D.). Monkeys were pair-housed when possible in climate-controlled conditions with 12-h light-dark cycles. Monkeys were provided water ad libitum and fed Teklad Global 20% Protein Primate Diet. For the experiment at the University of Kentucky, six male monkeys were used. After an overnight fast, monkeys were anaesthetized with ketamine (5 mg kg<sup>-1</sup>) and dexmedetomidine (0.0075–0.015 mg kg<sup>-1</sup>), and blood was collected from the femoral vein. The monkeys were then injected intravenously via the saphenous vein with either vehicle (PBS, USP-grade) or TRAF6i-HDL such that the dose of the CD40-TRAF6 inhibitor SMI 6877002 was 1 mg kg<sup>-1</sup>. Blood was collected at 15 min and at 6, 12, 24 and 48 h post injection. Following the blood draw, anaesthesia was reversed with atipamezole (0.075–0.15 mg kg<sup>-1</sup>). At 72 h post injection, fasted monkeys were anaesthetized with ketamine (25 mg kg<sup>-1</sup>), bled a final time, and euthanized by exsanguination with whole-body saline perfusion while anaesthetized with isoflurane (3–5% induction, 1–2% maintenance). Tissues were promptly removed and fixed in 10% neutral-buffered formalin. Blood was subjected to complete blood count test (ANTECH Diagnostics).

For the experiment at the Icahn School of Medicine at Mount Sinai, six female monkeys were used. For the <sup>89</sup>Zr-PET/MRI, animals were infused with 58.9  $\pm$  17.9 MBq of <sup>89</sup>Zr-labelled TRAF6i-HDL (1 mg kg<sup>-1</sup>) and imaged by PET/MRI at different time points. Dynamic PET imaging was performed during the first 60 min after infusion. Additional PET/MRI scans were performed at 24, 48 and 72 h. PET and MR images were acquired on a combined 3T PET/MRI system (Biograph mMR, Siemens Healthineers). On day 1, dynamic PET imaging was performed for 60 min using one bed position covering the chest and abdomen, directly after injection with <sup>89</sup>Zr-labelled TRAF6i-HDL. Simultaneously, anatomical vessel wall MR images were acquired using a proton density-weighted Sampling Perfection with Application optimized Contrasts using different flip angle Evolution (SPACE) sequence. MR imaging parameters were as follows: acquisition plane, coronal; repetition time, 1,000 ms; echo time, 79 ms; field of view, 300  $\times$  187 mm<sup>2</sup>; number of slices, 144; number of averages, 4; bandwidth, 601 Hz per pixel; turbo factor, 51; echo trains per slice, 4; echo train length, 192 ms; echo spacing, 3.7 ms; acquisition duration, 33 min and 36 s. After dynamic PET image acquisition, static whole-body PET images were acquired from the cranium to the pelvis, using 3 consecutive bed positions of 10 min each. Simultaneously with each bed, MR images were acquired as described above, except using only 1.4 signal average (acquisition duration, 11 min 44 s per bed). Whole-body PET and MR imaging was also performed at 24, 48 and 72 h after injection, using 3 bed positions (PET duration per bed, 30 min; MRI duration per bed, 33 min and 36 s). Whole-body MR images from each bed were automatically collated together by the scanner.

After acquisition, PET raw data from each bed were reconstructed and collated together offline using the Siemens proprietary e7tools with an Ordered Subset Expectation Maximization (OSEM) algorithm with Point Spread Function (PSF) correction. A dual-compartment (soft tissue and air) attenuation map was used for attenuation correction.

**Blood tests in non-human primates.** Blood was collected from non-human primates at 0 and 15 min and at 6, 12, 24, 28, 48 and 72 h after infusion. Serum was analysed using an Olympus AU400 Chemistry Analyzer. Whole-blood samples were also analysed using an IDEXX procyte DX Hematology Analyzer. Levels of IL-6, TNF- $\alpha$  and CCL2 were measured using the Milliplex detection

kits HCMP2MAG-19k and PRCYTOMAG-40k (Millipore). Samples were run in duplicate.

**Statistical analysis.** Continuous variables are expressed as the mean  $\pm$  standard deviation unless otherwise stated. Significance of differences were calculated using nonparametric Mann–Whitney U tests and Kruskal–Wallis tests. Probability values of  $P < 0.05$  were considered significant. Statistical analyses were performed using IBM Statistical Package for the Social Sciences (SPSS) version 25.

**Study approval.** All animal care, procedures and experiments were based on approved institutional protocols from the Icahn School of Medicine at Mount Sinai and the University of Kentucky Institutional Animal Care and Use Committee.

**Reporting Summary.** Further information on experimental design is available in the Nature Research Reporting Summary linked to this article.

**Data availability.** The authors declare that all data supporting the findings of this study are available within the paper and its Supplementary Information. RNA sequencing data are available at the Gene Expression Omnibus (GEO) database (GEO series number [GSE104777](https://www.ncbi.nlm.nih.gov/geo/query/acc.cgi?acc=GSE104777)).

Received: 19 September 2017; Accepted: 13 March 2018;

Published online: 16 April 2018

## References

- Swirski, F. K. & Nahrendorf, M. Leukocyte behavior in atherosclerosis, myocardial infarction, and heart failure. *Science* **339**, 161–166 (2013).
- Schönbeck, U. & Libby, P. CD40 signaling and plaque instability. *Circ. Res.* **89**, 1092–1103 (2001).
- Lutgens, E. et al. Requirement for CD154 in the progression of atherosclerosis. *Nat. Med.* **5**, 1313–1316 (1999).
- Mach, F., Schönbeck, U., Sukhova, G. K., Atkinson, E. & Libby, P. Reduction of atherosclerosis in mice by inhibition of CD40 signalling. *Nature* **394**, 200–203 (1998).
- Schönbeck, U., Sukhova, G. K., Shimizu, K., Mach, F. & Libby, P. Inhibition of CD40 signaling limits evolution of established atherosclerosis in mice. *Proc. Natl Acad. Sci. USA* **97**, 7458–7463 (2000).
- Lutgens, E. et al. Both early and delayed anti-CD40L antibody treatment induces a stable plaque phenotype. *Proc. Natl Acad. Sci. USA* **97**, 7464–7469 (2000).
- Lutgens, E. et al. Deficient CD40–TRAF6 signaling in leukocyte prevents atherosclerosis by skewing the immune response toward an anti-inflammatory profile. *J. Exp. Med.* **207**, 391–404 (2010).
- Zarzycka, B. et al. Discovery of small molecule CD40–TRAF6 inhibitors. *J. Chem. Inf. Model.* **55**, 294–307 (2015).
- Chatzigeorgiou, A. et al. Blocking CD40–TRAF6 signaling is a therapeutic target in obesity-associated insulin resistance. *Proc. Natl Acad. Sci. USA* **111**, 2686–2691 (2014).
- Robbins, C. S. et al. Local proliferation dominates lesional macrophage accumulation in atherosclerosis. *Nat. Med.* **19**, 1166–1172 (2013).
- Swirski, F. K. et al. Ly-6C<sup>hi</sup> monocytes dominate hypercholesterolemia-associated monocytes and give rise to macrophages in atheromata. *J. Clin. Invest.* **117**, 195–205 (2007).
- Swirski, F. K. et al. Monocyte accumulation in mouse atherogenesis is progressive and proportional to extent of disease. *Proc. Natl Acad. Sci. USA* **103**, 10340–10345 (2006).
- Kiener, P. A. et al. Stimulation of CD40 with purified soluble gp39 induces proinflammatory responses in human monocytes. *J. Immunol.* **155**, 4917–4925 (1995).
- Iloki Assanga, S. B. et al. Cell growth curves for different cell lines and their relationship with biological activities. *Int. J. Biotechnol. Mol. Biol. Res.* **4**, 60–70 (2013).
- Imhof, B. A. & Aurrand-Lions, M. Adhesion mechanisms regulating the migration of monocytes. *Nat. Rev. Immunol.* **4**, 432–444 (2004).
- Wenger, G. D. & O’Dorisio, M. S. Induction of cAMP-dependent protein kinase I during human monocyte differentiation. *J. Immunol.* **134**, 1836–1843 (1985).
- Chinetti-Gbaguidi, G., Colin, S. & Staels, B. Macrophage subsets in atherosclerosis. *Nat. Rev. Cardiol.* **12**, 10–17 (2015).
- Afford, S. C. et al. CD40 activation induces apoptosis in cultured human hepatocytes via induction of cell surface Fas ligand expression and amplifies Fas-mediated hepatocyte death during allograft rejection. *J. Exp. Med.* **189**, 441–446 (1999).
- Bhagal, R. H. et al. Activation of CD40 with platelet derived CD154 promotes reactive oxygen species dependent death of human hepatocytes during hypoxia and reoxygenation. *PLoS ONE* **7**, e30867 (2012).
- Tang, Y. et al. Up-regulation of the expression of costimulatory molecule CD40 in hepatocytes by hepatitis B virus X antigen. *Biochem. Biophys. Res. Commun.* **384**, 12–17 (2009).
- Kawai, T., Andrews, D., Colvin, R. B., Sachs, D. H. & Cosimi, A. B. Thromboembolic complications after treatment with monoclonal anti-body against CD40 ligand. *Nat. Med.* **6**, 114 (2000).
- André, P. et al. CD40L stabilizes arterial thrombi by a  $\beta 3$  integrin-dependent mechanism. *Nat. Med.* **8**, 247–252 (2002).
- Ahonen, C. et al. The CD40–TRAF6 axis controls affinity maturation and the generation of long-lived plasma cells. *Nat. Immunol.* **3**, 451–456 (2002).
- Duijvenvoorden, R. et al. A statin-loaded reconstituted high-density lipoprotein nanoparticle inhibits atherosclerotic plaque inflammation. *Nat. Commun.* **5**, 3065 (2014).
- Shah, P. K. et al. Effects of recombinant apolipoprotein A-I<sub>Milano</sub> on aortic atherosclerosis in apolipoprotein E-deficient mice. *Circulation* **97**, 780–785 (1998).
- Moore, K. J., Sheedy, F. J. & Fisher, E. A. Macrophages in atherosclerosis: a dynamic balance. *Nat. Rev. Immunol.* **13**, 709–721 (2013).
- Potteaux, S. et al. Suppressed monocyte recruitment drives macrophage removal from atherosclerotic plaques of *ApoE*<sup>-/-</sup> mice during disease regression. *J. Clin. Invest.* **121**, 2025–2036 (2011).
- Dutta, P. et al. Myocardial infarction accelerates atherosclerosis. *Nature* **487**, 325–329 (2012).
- Nissen, S. E. et al. Effect of recombinant ApoA-I Milano on coronary atherosclerosis in patients with acute coronary syndromes: a randomized controlled trial. *JAMA* **290**, 2292–2300 (2003).
- Tardif, J. C. et al. Effects of reconstituted high-density lipoprotein infusions on coronary atherosclerosis: a randomized controlled trial. *JAMA* **297**, 1675–1682 (2007).
- Lerch, P. G. et al. Production and characterization of a reconstituted high density lipoprotein for therapeutic applications. *Vox Sang.* **71**, 155–164 (1996).
- Nykiforuk, C. L. et al. Expression and recovery of biologically active recombinant Apolipoprotein A1<sub>Milano</sub> from transgenic safflower (*Carthamus tinctorius*) seeds. *Plant Biotechnol. J.* **9**, 250–263 (2011).
- Sanchez-Gaytan, B. L. et al. HDL-mimetic PLGA nanoparticle to target atherosclerosis plaque macrophages. *Bioconjug. Chem.* **26**, 443–451 (2015).
- Degoma, E. M. & Rader, D. J. Novel HDL-directed pharmacotherapeutic strategies. *Nat. Rev. Cardiol.* **8**, 266–277 (2011).
- Tardif, J. C. et al. Effect of rHDL on Atherosclerosis-Safety and Efficacy (ERASE) Investigators. Effects of reconstituted high-density lipoprotein infusions on coronary atherosclerosis: a randomized controlled trial. *JAMA* **297**, 1675–1682 (2007).
- Tardif, J. C. et al. Effects of the high-density lipoprotein mimetic agent CER-001 on coronary atherosclerosis in patients with acute coronary syndromes: a randomized trial. *Eur. Heart J.* **35**, 3277–3286 (2014).
- Kim, Y. et al. Single step reconstitution of multifunctional high-density lipoprotein-derived nanomaterials using microfluidics. *ACS Nano* **7**, 9975–9983 (2013).
- Pérez-Medina, C. et al. In vivo PET imaging of HDL in multiple atherosclerosis models. *JACC Cardiovasc. Imaging* **9**, 950–961 (2016).
- Ridker, P. M. et al. Rosuvastatin to prevent vascular events in men and women with elevated C-reactive protein. *N. Engl. J. Med.* **359**, 2195–2207 (2008).
- Everett, B. M. et al. Rationale and design of the Cardiovascular Inflammation Reduction Trial: a test of the inflammatory hypothesis of atherothrombosis. *Am. Heart J.* **166**, 199–207 (2013).
- Ridker, P. M. et al. Antiinflammatory therapy with canakinumab for atherosclerotic disease. *N. Engl. J. Med.* **377**, 1119–1131 (2017).
- Stone, G. W. et al. A prospective natural-history study of coronary atherosclerosis. *N. Engl. J. Med.* **364**, 226–235 (2011).
- Jonas, A. Reconstitution of high-density lipoproteins. *Methods Enzymol.* **128**, 553–582 (1986).
- Pérez-Medina, C. et al. PET imaging of tumor-associated macrophages with <sup>89</sup>Zr-labeled high-density lipoprotein nanoparticles. *J. Nucl. Med.* **56**, 1272–1277 (2015).
- Langmead, B. & Salzberg, S. L. Fast gapped-read alignment with Bowtie 2. *Nat. Methods* **9**, 357–359 (2012).
- Anders, S., Pyl, P. T. & Huber, W. HTSeq — a Python framework to work with high-throughput sequencing data. *Bioinformatics* **31**, 166–169 (2015).
- Mudge, J. M. & Harrow, J. Creating reference gene annotation for the mouse C57BL6/J genome assembly. *Mamm. Genome* **26**, 366–378 (2015).
- Ritchie, M. E. et al. Limma powers differential expression analyses for RNA-sequencing and microarray studies. *Nucleic Acids Res.* **43**, e47 (2015).
- Wang, J. et al. GO-function: deriving biologically relevant functions from statistically significant functions. *Brief. Bioinform.* **13**, 216–227 (2012).
- Kanehisa, M., Goto, S., Sato, Y., Furumichi, M. & Tanabe, M. KEGG for integration and interpretation of large-scale molecular data sets. *Nucleic Acids Res.* **40**, D109–D114 (2012).

## Acknowledgements

The authors thank the Icahn School of Medicine and the following Mount Sinai's core facilities: flow cytometry core, quantitative PCR core and TMII's preclinical imaging core. This study was funded by National Institutes of Health grants R01 HL118440, R01 HL125703 and P01 HL131478 (all to W.J.M.M.), R01 EB009638 (to Z.A.F.) and R01 HL144072 (to W.J.M.M. and Z.A.F.), as well as by NWO grants ZonMW Veni 016156059 (to R.D.) and ZonMW Vidi 91713324 (to W.J.M.M.), and by the European Research Council (ERC Con to E.L.) and by the DFG (SFB 1123-A5 to E.L.).

## Author contributions

R.D. and W.J.M.M. designed the study. R.D., M.L., T.B., M.M.T.v.L., M.L.S., J.T., T.T.P.S., J.K., E.S.G.S., J.O., E.A.F., R.E.T., N.K., P.R., A.K., F.K.S., M.N., Z.A.F., E.L. and W.J.M.M. designed, performed and oversaw the in vivo and ex vivo experiments. F.F., B.L.S.-G. and M.L. developed and produced TRAF6i-HDL. Flow cytometry, histology and immunostaining, laser capture microdissection, and blood chemistry experiments were performed and analysed by R.D., M.L., M.M.T.v.L. and J.M. FMT/CT was performed and analysed by R.D., Y.Y., G.W. and M.N. The RNA sequencing was performed and analysed by X.Z., B.Z., R.D. and M.L. Monocyte migration assays were performed by J.K. PET/CT

and pharmacokinetic studies in mice were performed by C.P.-M., J.T. and T.R. <sup>89</sup>Zr-PET/MRI in non-human primates was performed and analysed by T.B., M.L.S., C.P.-M. and C.C. The manuscript was written by R.D., M.L. and W.J.M.M. All authors contributed to the writing of the manuscript and approved the final draft. R.D., Z.A.F. and W.J.M.M. provided funding.

## Competing interests

These authors declare no competing interests.

## Additional information

**Supplementary information** is available for this paper at <https://doi.org/10.1038/s41551-018-0221-2>.

**Reprints and permissions information** is available at [www.nature.com/reprints](http://www.nature.com/reprints).

**Correspondence and requests for materials** should be addressed to W.J.M.M. or R.D.

**Publisher's note:** Springer Nature remains neutral with regard to jurisdictional claims in published maps and institutional affiliations.

## Life Sciences Reporting Summary

Nature Research wishes to improve the reproducibility of the work that we publish. This form is intended for publication with all accepted life science papers and provides structure for consistency and transparency in reporting. Every life science submission will use this form; some list items might not apply to an individual manuscript, but all fields must be completed for clarity.

For further information on the points included in this form, see [Reporting Life Sciences Research](#). For further information on Nature Research policies, including our [data availability policy](#), see [Authors & Referees](#) and the [Editorial Policy Checklist](#).

Please do not complete any field with "not applicable" or n/a. Refer to the help text for what text to use if an item is not relevant to your study. For final submission: please carefully check your responses for accuracy; you will not be able to make changes later.

### ▶ Experimental design

#### 1. Sample size

Describe how sample size was determined.

Calculations of sample size for the experiments in mice were based on previous experience, in particular on the measurements of drug effects on histological cross-sections of the aortic sinus area, in which macrophage area was measured (Duivenvoorden et al. Nat. Commun. 5, 3065 (2014)). This is similar to what we did in this study. We calculated that at least seven mice per group were needed to provide a statistical power of 80% to detect a difference of  $50 \times 10^3$   $\mu\text{m}$ , assuming a standard deviation of  $30 \times 10^3$   $\mu\text{m}$  and a two-sided alpha of 0.05. Therefore we included 8 to 10 mice per group. For the experiments with the non-human primates, no formal sample size calculation was made.

#### 2. Data exclusions

Describe any data exclusions.

No raw data were excluded.

#### 3. Replication

Describe the measures taken to verify the reproducibility of the experimental findings.

The reduction of plaque macrophages, as measured by flow cytometry, was detected in three separate experiments. All attempts at replication were successful.

#### 4. Randomization

Describe how samples/organisms/participants were allocated into experimental groups.

Animals were allocated into different treatment groups on the basis of randomly chosen cage numbers.

#### 5. Blinding

Describe whether the investigators were blinded to group allocation during data collection and/or analysis.

Group allocation was performed blinded. All sample processing and the histological analysis were performed without knowledge of group allocation.

Note: all in vivo studies must report how sample size was determined and whether blinding and randomization were used.

## 6. Statistical parameters

For all figures and tables that use statistical methods, confirm that the following items are present in relevant figure legends (or in the Methods section if additional space is needed).

- n/a Confirmed
- The exact sample size ( $n$ ) for each experimental group/condition, given as a discrete number and unit of measurement (animals, litters, cultures, etc.)
  - A description of how samples were collected, noting whether measurements were taken from distinct samples or whether the same sample was measured repeatedly
  - A statement indicating how many times each experiment was replicated
  - The statistical test(s) used and whether they are one- or two-sided  
*Only common tests should be described solely by name; describe more complex techniques in the Methods section.*
  - A description of any assumptions or corrections, such as an adjustment for multiple comparisons
  - Test values indicating whether an effect is present  
*Provide confidence intervals or give results of significance tests (e.g.  $P$  values) as exact values whenever appropriate and with effect sizes noted.*
  - A clear description of statistics including central tendency (e.g. median, mean) and variation (e.g. standard deviation, interquartile range)
  - Clearly defined error bars in all relevant figure captions (with explicit mention of central tendency and variation)

See the web collection on [statistics for biologists](#) for further resources and guidance.

## ► Software

Policy information about [availability of computer code](#)

### 7. Software

Describe the software used to analyze the data in this study.

Statistical package for the social sciences (SPSS). Siemens proprietary e7 tools. Inveon Research Workplace. OsiriX v.6.5.2. Bioconductor package limma. FlowJo v10.0.7. Graphpad Prism. ImageJ. Adobe Photoshop. Xenogen Living Image. ASIPro VMTM. Bowtie2 version 2.3. HTSeq version 0.6.1.

For manuscripts utilizing custom algorithms or software that are central to the paper but not yet described in the published literature, software must be made available to editors and reviewers upon request. We strongly encourage code deposition in a community repository (e.g. GitHub). [Nature Methods guidance for providing algorithms and software for publication](#) provides further information on this topic.

## ► Materials and reagents

Policy information about [availability of materials](#)

### 8. Materials availability

Indicate whether there are restrictions on availability of unique materials or if these materials are only available for distribution by a third party.

No restrictions on the availability of unique materials.

### 9. Antibodies

Describe the antibodies used and how they were validated for use in the system under study (i.e. assay and species).

The following antibodies were used: F4/80-PE-Cy7 (clone BM8, BioLegend, cat# 123114, dilution 1:200); CD11b-PerCP/Cy5.5 (clone M1/70, BioLegend, cat#101208, dilution 1:200); CD11c-APC (clone N418, BioLegend, cat# 117310, dilution 1:200); CD45-brilliantviolet510 (clone 30-F11, BioLegend, cat#103138, 1:200); Ly-6C-PE (clone AL-21, BD Biosciences, cat#560592, dilution 1:200); Ly6C-FITC (clone AL-21, BD Biosciences, cat#553104, dilution 1:200); CD90.2-eFluor450 (clone 53-2.1, eBioscience, cat#48-0902-82, dilution 1:200); CD90.2-PE (clone 53-2.1, BD Biosciences, cat#12-0902-82, 1:200); Ter119-eFluor450 (clone TER-119, eBioscience, cat#48-5921-82, dilution 1:200); NK1.1-eFluor450 (clone PK136, eBioscience, cat#48-5941-82, dilution 1:200); NK1.1-PE (clone PK136, BD Biosciences, cat#12-5941-82, dilution 82); CD49b-eFluor450 (clone DX5, eBioscience, cat#48-5971-82, dilution 1:200); CD45R-eFluor450 (clone RA3-6B2, eBioscience, cat#48-0452-82, dilution 1:200); Ly-6G-PacificBlue (clone 1A8, BioLegend, cat# 127612, dilution 1:100); Ly-6G-PE (clone 1A8, BD Biosciences, cat#561104, dilution 1:100); CD3-PE (clone 17A2, BioLegend, cat#100206, dilution 1:200); CD19-PE (clone 1D3, BD Bioscience, cat#553786, dilution 1:200); Anti-BrdU (BD APC-BrdU Kit, cat#552598, dilution 1:50); Fc-block (clone 2.4G2, BD Biosciences, cat#553142, dilution 1:200). Every antibody used was validated for flow-cytometry applications.

## 10. Eukaryotic cell lines

a. State the source of each eukaryotic cell line used.

Human Arterial Endothelial Cells (HAEC, purchased from Lonza (Baltimore,MD)).  
Human blood monocytes were isolated from fresh healthy donor samples,  
provided by the AMC hospital bloodbank.

b. Describe the method of cell line authentication used.

None of the cell lines were authenticated.

c. Report whether the cell lines were tested for mycoplasma contamination.

Cell lines were tested for mycoplasma contamination.

d. If any of the cell lines used are listed in the database of commonly misidentified cell lines maintained by [ICLAC](#), provide a scientific rationale for their use.

No commonly misidentified cell lines were used.

## ► Animals and human research participants

Policy information about [studies involving animals](#); when reporting animal research, follow the [ARRIVE guidelines](#)

## 11. Description of research animals

Provide all relevant details on animals and/or animal-derived materials used in the study.

Female Apoe<sup>-/-</sup> mice (B6.129P2-Apoetm1Unc), 8 weeks old.  
Adult male cynomolgus monkeys (Macacafascicularis).

Policy information about [studies involving human research participants](#)

## 12. Description of human research participants

Describe the covariate-relevant population characteristics of the human research participants.

The study did not involve human research participants.